April 11, 2006 Version 1.2

An Ultraviolet-to-Radio Broadband Spectral Atlas of Nearby Galaxies

D.A. Dale[1], A. Gil de Paz[2], G.J. Bendo[3], L. Bianchi[4], S. Boissier[5], D. Calzetti[6], C.W. Engelbracht[7], K.D. Gordon[7], H.M. Hanson[1], G. Helou[8], R.C. Kennicutt[9,6], B.F. Madore[4], D.C. Martin[10], M.J. Meyer[6], M.W. Regan[6], M.L. Sosey[6] et al.

ABSTRACT

The ultraviolet-to-radio continuum spectral energy distributions are presented for all 75 galaxies in the *Spitzer* Infrared Nearby Galaxies Survey. A principal component analysis of the sample shows that most of the sample's spectral variations stem from two underlying components, one representative of a galaxy with a low infrared-to-ultraviolet ratio and one representative of a galaxy with a high infrared-to-ultraviolet ratio. The influence of several parameters on the infrared-to-ultraviolet ratio is studied (e.g., optical morphology, disk inclination, far-infrared color, ultraviolet spectral slope). Similar to previous findings on normal star-forming galaxies, compared to starbursting galaxies the SINGS sample shows a larger dispersion in a plot of infrared-to-ultraviolet versus ultraviolet spectral slope. Much of this dispersion derives from the quiescent, early-type galaxies in the SINGS sample, which show significantly redder ultraviolet spectral slopes than do starbursts at a given infrared-to-ultraviolet ratio. Finish abstract with new discovery that the wedge-shaped distribution in IR/UV vs 70/160 can be explained with 24 μm morphology.

Subject headings: infrared: galaxies — infrared: ISM

[1]Department of Physics and Astronomy, University of Wyoming, Laramie, WY 82071; ddale@uwyo.edu

[2]Departamento de Astrofisica, Universidad Complutense, Avenida de la Complutense s/n, Madrid, E-28040, Spain

[3]Astrophysics Group, Imperial College, Blackett Laboratory, Prince Consort Road, London SW7 2AZ United Kingdom

[4]Department of Physics & Astronomy, Johns Hopkins University, Charles & 34$^{\rm th}$ Street, Baltimore, MD 21218

[5]Carnegie Observatories, Carnegie Institution of Washington, 813 Santa Barbara Street, Pasadena, CA 91101

[6]Space Telescope Science Institute, 3700 San Martin Drive, Baltimore, MD 21218

[7]Steward Observatory, University of Arizona, 933 North Cherry Avenue, Tucson, AZ 85721

[8]California Institute of Technology, MC 314-6, Pasadena, CA 91101

[9]Institute of Astronomy, University of Cambridge, Cambridge CB3 0HA, United Kingdom

[10]Astronomy Option, California Institue of Technology, MS 105-24, Pasadena, CA 91125

1. Introduction

Dust has always presented challenges to astronomy. Extinction makes it difficult to extract intrinsic fluxes. Reddening leads to uncertain colors. An outstanding challenge is to identify dust emission features that were discovered over 80 years ago. Nonetheless, interstellar dust also provides unique opportunities for understanding galaxy structure and evolution. The formation of molecules, interstellar heating and cooling processes, polarization, and photometric redshift indicators are just a few of the areas of study that benefit from the presence and knowledge of interstellar grains (see Draine 2003 for a review).

Though dust primarily releases energy over infrared and submillimeter wavelengths, much of the radiation intercepted by interstellar grains originates in the ultraviolet from the atmospheres of OB stars. Thus the combination of infrared and ultraviolet data presents interesting challenges and opportunities. One important application is determining ultraviolet-based star formation rates corrected for dust extinction. High redshift surveys carried out in the rest-frame ultraviolet and optical, for example, are particularly vulnerable to the presence of interstellar dust (e.g., Adelberger & Steidel 2000). Fortunately, studies coupling infrared and ultraviolet data have shown that the slope of the ultraviolet continuum is one such useful probe of the extinction in starburst galaxies (e.g., Meurer et al. 1999; Gordon et al. 2000). Subsequent work in this area has explored how the infrared-to-ultraviolet ratio and its scatter depend on bolometric and monochromatic luminosity, ultraviolet spectral slope, metallicity, diameter, star formation rate, etc. (e.g., Buat et al. 2002; Bell 2003; Gordon et al. 2004; Kong et al. 2004; Buat et al. 2005; Calzetti et al. 2005; Seibert et al. 2005; Cortese et al. 2006; Schmitt et al. 2006; Iglesias-Páramo et al. 2006). One consistent result relevant to the work presented below is that normal star-forming (non-starburst) galaxies show larger scatter in plots of the infrared-to-ultraviolet ratio as a function of the ultraviolet spectral slope, with normal galaxies systematically exhibiting redder slopes. This broadening in the trend has been attributed to geometry and/or the increased fractional contributions from recent (versus current) star formation (e.g., Bell et al. 2002; Kong et al. 2004; Calzetti et al. 2005; Siebert 2005).

We are interested in exploring how the infrared-to-ultraviolet ratio depends on quantities like morphology, color, and geometry within the SINGS sample (Kennicutt et al. 2003). But in broader terms, the main focus of this paper is to simply present a panchromatic atlas of the broadband spectral energy distributions of a large, diverse sample of nearby galaxies, and to quantify the variety of spectral shapes evident in such a sample. Since the fluxes presented in this work span wavelengths from the far-ultraviolet to the radio and are integrated over entire galaxies, this dataset should prove useful to astronomers studying galaxies at high redshifts, where only information on the global properties of galaxies is accessible and the rest-frame ultraviolet data are shifted into optical bandpasses. One may plausibly argue that the variety of luminosities and spectral shapes typically seen in high redshift surveys will be narrower than the diversity presented below for the SINGS sample, since flux-limited surveys at high redshifts will mainly be sampling luminous and infrared-warm systems. On the other hand, deep far-infrared surveys show significant numbers of higher redshift systems similar to local normal star-forming galaxies in mass, size, and dust

temperature (e.g., Chapman et al. 2002; Sajina et al. 2006). In either case, the rich collection of *Spitzer* and ancillary data provided by the SINGS project represents an important panchromatic baseline for extragalactic work. Below we present global fluxes at ultraviolet, optical, near-infrared, infrared, submillimeter, and radio wavelengths for the 75 SINGS galaxies.

2. The Sample

The 75 galaxies in the *Spitzer* Nearby Galaxies Survey (SINGS; Kennicutt et al. 2003) come from a wide range of environments and galaxy types: low-metallicity dwarfs; quiescent ellipticals; dusty grand design spirals; Seyferts, LINERs, and star-forming nuclei of normal galaxies; and systems within the Local and M 81 groups. The selection of the collection of 75 SINGS galaxies aimed to span a wide range in three key parameters (optical morphology, luminosity, infrared-to-optical color) and to span a wide range in several other secondary parameters (e.g., infrared color, metallicity, surface brightness, inclination, bar structure, etc.). The SINGS sample is comprised of nearby galaxies, with a median distance of ∼10 Mpc and a maximum distance of only 30 Mpc.

3. The Data

Tables 1-3 present the global flux densities for the entire SINGS sample, for wavelengths spanning the ultraviolet through the radio. A full description of the infrared and submillimeter data can be found in Dale et al. (2005). Unlike the presentation in Dale et al. (2005), Table 1 includes the extended source aperture corrections given in Reach et al. (2005) for IRAC flux densities, multiplicative factors of [0.944,0.937,0.772,0.737] at wavelengths [3.6,4.5,5.8,8.0] (μm). The data are also corrected for Galactic extinction (Schlegel, Finkbeiner, & Davis 1998) assuming $A_V/E(B-V) \approx 3.1$ and the extinction curve of Li & Draine (2001). Below follows a description of the new ultraviolet and optical and archival radio data collected for the SINGS program.

3.1. Ultraviolet Data

The GALEX mission (Martin et al. 2005) is performing an all-sky survey at ultraviolet wavelengths. The imaging portion of the survey is being carried out with a far-ultraviolet and a near-ultraviolet filter respectively centered at 1528 and 2271 Å. In addition to imaging the entire sky with an effective exposure time of ∼0.1 ksec, GALEX is also carrying relatively deep integrations (∼1.5 ksec) for a few hundred nearby galaxies, including the entire SINGS sample. With an angular resolution of 4-6″, the spatial details in GALEX images are well matched to those seen in *Spitzer* 24 μm imaging and more resolved than in *Spitzer* 70 and 160 μm images. This resolution coupled with the GALEX field-of-view of 1.°25 allow for robust measures of sky-subtracted, integrated ultraviolet fluxes even for large nearby galaxies.

Integrated ultraviolet fluxes are computed from the surface photometry profiles derived for the GALEX Atlas of Nearby Galaxies (Gil de Paz et al. 2006, in preparation). Table 2 lists the global fluxes that include an asymptotic extrapolation to the isophotal profiles. The extrapolations are typically small and result in asymptotic fluxes that are, on average, 14% larger than those obtained at the optical radius; $\langle f_{\rm UV}({\rm asymptotic})/f_{\rm UV}(R_{25})\rangle = 1.14$ with a dispersion of 0.16 and 0.14 in the far- and near-ultraviolet, respectively. The fluxes have been corrected for the Galactic extinction listed for each source on NED[1]. Some of the SINGS galaxies have not yet been observed, and a few that only have near-ultraviolet observations because the far-ultraviolet detector was turned off at that time (see Table 2). There are a few sources for which there are restrictions (e.g., bright nearby stars) that make it unlikely GALEX will obtain data. *Armando: please let me know which ones will never be observed.*

The uncertainties listed in Table 2 include the formal uncertainties from the weighted fits to the growth curves using the uncertainties of the individual points in the growth curves, in addition to absolute calibration uncertainties of ∼15% in both the far- and near-ultraviolet.

3.2. Optical Data

The optical imaging for the SINGS project was carried out over the course of five observing runs at the Kitt Peak National Observatory 2.1 m and one observing run at the Cerro Tololo Inter-American Observatory 1.5 m telescopes between March 2001 and February 2003. Broadband photometry was obtained in BVRI using 2K×2K CCDs with pixel scales and fields-of-view of $0\farcs305$ and $10'$ at KPNO and $0\farcs433$ and $14\farcm5$ at CTIO. Galaxies more extended than the CCD fields-of-view were imaged at multiple, overlapping pointings. Typical exposure times were 1440 s (B), 720 s (V), 420 s (R), and 840 s (I), usually split into two separate exposures to aid cosmic ray removal. Such exposures reach a depth of about 25 mag arcsec^{-2} at a signal-to-noise ratio of ∼10.

Data processing consisted of standard routines such as bias subtraction, flat-fielding with both dome- and twilight-flats, cosmic ray removal, and the mosaicking of overlapping pointings for galaxies with large angular extents. The southern $3'$ of the KPNO 2.1 m CCD field-of-view suffers from vignetting; care was taken to remove as much of the vignetted portion of the KPNO images as feasible. Photometric standard stars were observed during each observing run to flux calibrate the images. Most images have photometric accuracy of 5% or better.

Global optical fluxes were extracted using the same apertures that were used for the IRAC and MIPS global flux extractions; these apertures cover at least the entire optical disk. Sky estimation and subtraction was carried out through the use of multiple sky apertures placed near the source without overlapping the faintest isophotes visible from the galaxy. Foreground stars were edited from the optical images after first being conservatively identified using $f_\nu(3.6\ \mu{\rm m})/f_\nu(8.0\ \mu{\rm m})$ and

[1]NASA/IPAC Extragalactic Database

$f_\nu(8.0\ \mu\mathrm{m})/f_\nu(24\ \mu\mathrm{m})$ color images.

3.3. Radio Data

Global 20 cm continuum fluxes from the literature are available for 62 SINGS galaxies, with data for 53 of of these galaxies taken from the New VLA Sky Survey catalog (Condon 1998; Yun, Reddy, & Condon 2001; see Table 3). Although this is a snapshot survey and prone to miss extended emission from galaxies having large angular extents, proper attention has been paid to these effects to derive unbiased 1.4 GHz fluxes (e.g., Yun, Reddy, & Condon 2001).

4. Results

4.1. Global Broadband Spectral Energy Distributions

Figures 1-8 show the ultraviolet-to-submillimeter spectral energy distributions for the SINGS sample. The solid curve is the sum of a dust (dashed) and a stellar (dotted) model. The dust curve is a Dale & Helou (2002) model fitted to the 24, 70, and 160 μm fluxes; the α_{SED} listed within each panel parametrizes the distribution of dust mass as a function of heating intensity, as described in Dale & Helou (2002). The stellar curve is the 900 Myr continuous star formation, solar metallicity, Salpeter IMF ($\alpha_{\mathrm{IMF}} = 2.35$) curve from Vazquez & Leitherer (2005) fitted to the 2MASS data. The stellar curve is included as a "standard" reference against which the deviations in the ultraviolet and optical data, from the stellar curve, can be compared from galaxy to galaxy.

4.2. Spectral Energy Distributions Binned by the Infrared-to-Ultraviolet Ratio

Spatially-resolved panchromatic surveys of galaxies at high redshift ($z \gtrsim 1$) are beyond the reach of present technology. Analysis of the distribution of global (spatially-integrated) spectral energy distributions is a sensible starting point for current cosmology surveys (e.g., Rowan-Robinson et al. 2005). Figure 9 shows a stack of SINGS spectral energy distributions that emphasizes the infrared-to-ultraviolet variations within the SINGS sample. Each spectral energy distribution in the stack represents an average of approximately 10 individual spectral energy distributions that fall within a given bin of the total infrared-to-ultraviolet ratio, where "total infrared" implies just the dust continuum emission between 3 and 1100 μm (see Dale et al. 2001; Dale & Helou 2002). The spectra are arbitrarily normalized at the 2MASS K band wavelength.

Several features in the stack are immediately noticeable. The ultraviolet slopes vary from positive values for galaxies with high infrared/ultraviolet ratios to negative values for low infrared/ultraviolet ratio galaxies (as will be explored in detail in § 5.4). The 4000Å break shows up quite clearly, even at this coarse spectral "resolution." Other obvious features include: the broad

far-infrared peak signifying emission from cool-to-warm large grains; the contributions from polycyclic aromatic hydrocarbons appearing as mid-infrared emission features; and the near-infrared bump arising from photosheric emission from old stellar populations. Note also the broad spread in the ultraviolet data compared to that in the far-infrared. The variations in the infrared-to-ultraviolet ratio studied later in this work are largely driven by variations in the ultraviolet emission.

Close inspection of Figure 9 reveals that most of the variation in the stacked spectra stem from the two extreme bins (bins "1" and "6") in the infrared-to-ultraviolet ratio. However, substantial variations are still seen in bins 2-5 at ultraviolet and mid-infrared wavelengths. The bin 2-5 spread is 0.90, 0.78, 0.30, and 0.35 dex at 0.15, 0.23, 8.0, and 24 μm (compared to the full spreads of 1.78, 1.74, 0.64, and 0.69 dex over bins 1-6 at the same wavelengths). The spread at ultraviolet wavelengths is presumably significantly affected by variations in dust content. The range in 8.0 μm emission, on the other hand, is likely due to PAH destruction/formation variations. Low metallicity systems, for example, are known to be deficient in PAH emission (e.g., Dale et al. 2005; Engelbracht et al. 2005; Galliano et al. 2005). The 24 μm emission from galaxies is known to be sensitive to the star formation rate (e.g., Dale et al. 2005; Gordon et al. 2004; Helou et al. 2004; Hinz et al. 2004); the observed variations at this wavelength may be strongly affected by the range in the sample's star formation properties.

4.3. Principal Component Analysis

A principal component analysis can help to quantify relative contributions to the observed variations in a sample of spectral energy distributions (Deeming 1964). A set of i eigenvectors $\{\vec{e_i}\}$ and their corresponding eigenvalues $\{e_i\}$ for our sample of N galaxies are computed from a diagonalization of the covariance matrix

$$C_{jk} = \frac{1}{N}\Sigma_{i=1}^{N}\, \nu f_\nu^i(\lambda_j)\, \nu f_\nu^i(\lambda_k), \tag{1}$$

where $\nu f_\nu^i(\lambda_j)$ is the flux of the $i^{\rm th}$ spectrum at wavelength λ_j. We restrict the computation of the covariance matrix to involve only those wavelengths for which we have a substantial database of fluxes; submillimeter data at 450 and 850 μm are not included in the principal component analysis. Furthermore, to avoid spurious results we do not include in our analysis any SINGS galaxies without a secure detection/measurement at any of the ultraviolet, optical, near-infrared, or infrared wavelengths listed in Tables 1-2. Hence, our principal component analysis involves only about half of the SINGS sample[2] and does not include many of the dwarf/irregular systems and is thus biased towards the brighter galaxies. Our principal component analysis is carried out after normalizing the spectra at the 2MASS K_s band wavelength.

[2]SINGS/GALEX reader: N(principal component) currently equals 36, but this number should rise as we obtain more GALEX data and as we progress on optical flux calibration work for Data Release 4.

The two largest eigenvalues e_1 and e_2 correspond to the eigenvectors $\vec{e}_1$ and $\vec{e}_2$ that describe most of the variation in the spectral atlas. Normalizing the eigenvalues by their sum, $e'_i = e_i/\Sigma_j e_j$, shows that $\vec{e}_1$ and $\vec{e}_2$ respectively contribute to 85% and 10% of the observed variation in the sample spectra (i.e., $e'_1 = 0.85$ and $e'_2 = 0.10$; the remaining normalized eigenvalues are individually no larger than 0.02). To quantify the uncertainty on these numbers, we have performed 10,000 Monte Carlo simulations of the principal component analysis. For each simulation we use the tabulated flux uncertainties to add a random (Gaussian deviate) flux offset to every galaxy's flux at each wavelength. The means of the two largest normalized eigenvalues from these simulations are $\langle e'_1 \rangle = 0.84 \pm 0.01$ and $\langle e'_2 \rangle = 0.10 \pm 0.01$, with the error bars reflecting the 1σ standard deviation from the simulations. The means of the two primary eigenvectors, $\langle \vec{e}_1 \rangle$ and $\langle \vec{e}_2 \rangle$, are displayed in Figure 10. Eigenvector $\langle \vec{e}_1 \rangle$ is indicative of a galaxy with a low infrared-to-ultraviolet ratio, whereas $\langle \vec{e}_2 \rangle$ represents a high infrared-to-ultraviolet spectrum. The error bars shown in Figure 10 portray the 1σ dispersions for each data point from the simulations.

5. The Infrared-to-Ultraviolet Ratio

What drives the variations in the infrared-to-ultraviolet ratio in galaxies? Which parameters can be used to quantify these variations, with the aim of simplifying SED analysis? Various possibilities are presented and discussed below.

5.1. Inclination

The tilt of a spiral disk with respect to the observer's line of sight affects the observed intensity and colors (e.g., Bruzual, Magris, & Calvet 1988; Boselli & Gavazzi 1994; Giovanelli et al. 1995; Kuchinski et al. 1998). The "disk" inclination can be computed from the observed semi-major and semi-minor axes, a and b, assuming that disks are oblate spheroids with intrinsic axial ratio $(b/a)_{\rm int}$ using the relation:

$$\cos^2 i = \frac{(b/a)^2 - (b/a)^2_{\rm int}}{1 - (b/a)^2_{\rm int}}, \tag{2}$$

where $(b/a)_{\rm int} \simeq 0.2$ for morphological types earlier than Sbc and $(b/a)_{\rm int} \simeq 0.13$ otherwise (see Dale et al. 1997 and references therein). Figure 11 gives the infrared-to-ultraviolet ratio as a function of galaxy "disk" inclination. Galaxies with elliptical morphologies have not been included in the plot. The ratio does not obviously trend with galaxy orientation.

5.2. Morphology

Figure 12 displays the infrared-to-ultraviolet ratio as a function of galaxy optical morphology. In general, the ultraviolet light increases in importance as the morphology changes from early-

type spirals to late-type spirals to irregulars, reflecting the changing significance of star formation and the ultraviolet luminosity to the overall energy budget in galaxies. However, elliptical and S0 galaxies do not follow this general trend; some ellipticals and S0s show comparatively low infrared-to-ultraviolet ratios. This deviation to low infrared-to-ultraviolet ratios for some of the earliest-type galaxies is either due to a relative paucity of dust emission or a relative excess of ultraviolet emission. The former scenario is supported by a global energetic argument, as the infrared portion of the bolometric luminosity in ellipticals is typically only a few percent (Xilouris et al. 2004). Alternatively, some elliptical systems are conspicuous ultraviolet emitters, with the emission thought to mainly arise from low-mass, helium-burning stars from the extreme horizontal branch and later phases of stellar evolution (see O'Connell 1999 for a review). Residual, low-level star formation could also contribute to the ultraviolet emission in early type galaxies (reference). Recent evidence shows that strong ultraviolet emitters are the largest contributers to the significant scatter in the ultraviolet colors of early type galaxies (e.g., Yi et al. 2005; Rich et al. 2005). *Note to DAD: perhaps use different symbols for I0 and Im; I0 implies generally amorphous, whereas Im is more structurally specific (e.g., off-center bars, stochastic SF, features typically found in low-mass galaxies).*

This wide range in the fractional ultraviolet luminosity also leads to significant scatter in the infrared-to-ultraviolet ratio. Though the statistics are based on small numbers, a similarly large dispersion is seen for irregular systems at the other end of the morphological spectrum. Part of this dispersion is likely associated with the metal content in irregular/dwarf systems. Continuum emission from low-metallicity galaxies experiences less line blanketing which leads to harder radiation fields. Many of the dwarf and irregular systems in the SINGS sample indeed have elevated $f_\nu(70\mu\mathrm{m})/f_\nu(160\mu\mathrm{m})$ ratios (e.g., Dale et al. 2005; Fabian et al. 2006) that indicating strong overall heating of the dust grain population, resulting in comparatively high infrared-to-ultraviolet ratios.

5.3. Far-Infrared Color

The elevated far-infrared colors for SINGS dwarfs/irregulars are shown in Figure 13. An interesting feature in this plot is the apparent cone-shaped distribution, with a progressively smaller range in the infrared-to-ultraviolet ratio for cooler far-infrared colors. There is no obvious trend in $f_\nu(70\mu\mathrm{m})/f_\nu(160\mu\mathrm{m})$ with disk inclination, so it is unlikely that the disribution in Figure 13 is due to disk orientation. However, geometry may play a key role in creating this distribution. Perhaps galaxies with relatively high $f_\nu(70\mu\mathrm{m})/f_\nu(160\mu\mathrm{m})$ ratios have hotter dust since the dust is near sites of active star formation. Moreover, galaxies that appear as several bright clumps in the infrared provide a large number of 'clean' lines-of-sight from which ultraviolet photons may escape. Such clumpy galaxies would hence show comparatively low infrared-to-ultraviolet ratios. On the other hand, ultraviolet photons from galaxies that appear as a single point-like blob of nuclear emission would encounter significant extinction, and hence such galaxies would exhibit

high infrared-to-ultraviolet ratios. In contrast to hot dust systems, galaxies with relatively low $f_\nu(70\mu\mathrm{m})/f_\nu(160\mu\mathrm{m})$ ratios have cooler dust because the dust is not in spatial proximity of the hot stars (e.g., Panagia 1973). The heating of dust via the weaker ambient interstellar radiation field would be fractionally higher in these galaxies. Therefore, their morphological appearance in the infrared should be comparatively smooth.

Since the relative distribution of interstellar grains and their heating sources is central to the scenario outlined above, we turn to the 24 μm imaging to provide a test. MIPS 24 μm data may be uniquely suited for such a test, as the data trace both interstellar grains and their heating sources, and have significantly higher spatial resolution than either 70 or 160 μm imaging. In Figure **??**...

Regardless of the interpretation, the distribution in Figure 13 points to an empirical result that cooler systems show a constricted range of infrared-to-ultraviolet ratios.

5.4. Ultraviolet Spectral Slope

The infrared-to-ultraviolet ratio has been shown to be fairly tightly correlated with the ultraviolet spectral slope in starburst galaxies, an important discovery that allows the extinction at ultraviolet wavelengths to be estimated from ultraviolet spectral data (e.g., Meurer, Heckman, & Calzetti 1999). Non-starbursting galaxies have also been studied in this context, but their data show a larger dispersion, with normal star-forming and quiescent systems exhibiting redder ultraviolet spectra and/or lower infrared-to-ultraviolet ratios (e.g., Buat et al. 2002; Bell 2002; Kong et al. 2004; Gordon et al. 2004; Buat et al. 2005; Calzetti et al. 2005; Seibert et al. 2005; Cortese et al. 2006). The intrinsic ultraviolet spectral slope is quite sensitive to the effective age of the stellar population, leading Calzetti et al. (2005) to suggest that the evolved, non-ionizing stellar population ($\sim$50-100 Myr) dominates the ultraviolet emission in normal systems, in contrast to current star formation processes dominating the ultraviolet emisison in starbursts. The increased diversity in the ultraviolet spectral slopes for evolved stellar populations manifests itelf as an increased dispersion for quiescent and normal star-forming galaxies in plots of the infrared-to-ultraviolet ratio as a function of ultraviolet spectral slope.

Figure 14 displays such a diagram for this study. Normal star-forming and starbursting galaxies from Kong et al. (2004) and Calzetti et al. (1995) are plotted in addition to the SINGS data points. The dotted curve is that for starbursting galaxies from Kong et al. (2004) and the solid curve is applicable to normal star-forming galaxies (Cortese et al. 2006). Similar to what has been found for other samples of non-starbursting galaxies, the SINGS dataset shows more scatter in this diagram and the galaxies are redder in their ultraviolet spectral slope compared to starburst galaxies. Inspection of the distribution as a function of SINGS optical morphology, however, shows that the 11 reddest SINGS galaxies are type Sab or earlier; the early type galaxies in SINGS contribute to most of the observed scatter.

6. Summary

Summarize the results. Add that there is a connection between the principal component analysis and the fact that early-type SINGS galaxies contribute to much of the dispersion in the IR/UV versus UV slope diagram.

Support for this work, part of the *Spitzer Space Telescope* Legacy Science Program, was provided by NASA through Contract Number 1224769 issued by the Jet Propulsion Laboratory, California Institute of Technology under NASA contract 1407. We are thankful for the hard work put in by the instrument teams and the *Spitzer* Science Center. We gratefully acknowledge NASA's support for construction, operation, and science analysis for the GALEX mission, developed in cooperation with the Centre National d'Etudes Spatiales of France and the Korean Ministry of Science and Technology. This research has made use of the NASA/IPAC Extragalactic Database which is operated by JPL/Caltech, under contract with NASA. This publication makes use of data products from the Two Micron All Sky Survey, which is a joint project of the University of Massachusetts and IPAC/Caltech, funded by NASA and the National Science Foundation.

REFERENCES

Adelberger, K.L. & Steidel, C.C. 2000, ApJ, 544, 218

Bauer, F.E., Condon, J.J., Thuan, T.X., & Broderick, J.J. 2000, ApJS, 129, 547

Bell, E.F. 2002, ApJ, 577, 150

Bell, E.F., Gordon, K.D., Kennicutt, R.C., & Zaritsky, D. 2002, ApJ, 565, 994

Bell, E.F. 2003, ApJ, 586, 794

Boselli, A., & Gavazzi, G. 1994, A&A, 283, 12

Bruzual A., G., Magris, G., & Calvet, N. 1998, ApJ, 333, 673

Buat, V., Boselli, A., Gavazzi, G., & Bonfanti, C. 2002, A&A, 383, 801

Buat, V. et al. 2005, ApJ, 619, L51

Calzetti, D., Bohlin, R.C., Kinney, A.L., Storchi-Bergmann, T., & Heckman, T.M. 1995, ApJ, 443, 136

Calzetti, D. et al. 2005, ApJ, 633, 871

Chapman, S.C., Smail, I., Ivison, R.J., Helou, G., Dale, D.A., & Lagache, G. 2002, ApJ, 573, 66

Condon, J.J., Helou, G., Sanders, D.B., & Soifer, B.T. 1990, ApJS, 73, 359

Condon, J.J. 1987, ApJS, 65, 485

Condon, J.J., Cotton, W.D., Greisen, E.W., Yin, Q.F., Perley, R.A., Taylor, G.B., & Broderick, J.J. 1998, AJ, 115, 1693

Cortese, L., Boselli, A., Buat, V., Gavazzi, G., Boissier, S., Gil de Paz, A., Seibert, M., Madore, B.F., & Martin, C. 2006, ApJ, 637, 242

Dale, D.A., Giovanelli, R., Haynes, M.P., Scodeggio, M., Hardy, E., & Campusano, L.E. 1997, AJ, 114, 455

Dale, D.A., Helou, G., Contursi, A., Silbermann, N.A., & Kolhatkar, S. 2001, ApJ, 549, 215

Dale, D.A. & Helou, G. 2002, ApJ, 576, 159

Dale, D.A. et al. 2005, ApJ, 633, 857

Deeming, T.F. 1964, MNRAS, 127, 493

Draine, B.T. 2003, ARA&A, 41, 241

Engelbracht, C.W., Gordon, K.D., Rieke, G.H., Werner, M.W., Dale, D.A., & Latter, W.B. 2005, ApJ, 628, L29

Galliano, F., Madden, S.C., Jones, A.P., Wilson, C.D., & Bernard, J.P. 2005, A&A, 434, 867

Giovanelli, R., Haynes, M.P., Salzer, J.J., Wegner, G., da Costa, L.N., & Freudling, W. 1995, AJ, 110, 1059

Gordon, K.D., Clayton, G.C., Witt, A.N., & Misselt, K.A. 2000, ApJ, 533, 236

Gordon, K. et al. 2004, ApJS, 154, 215

Helou, G. et al. 2004, ApJS, 154, 253

Hinz, et al. 2004, ApJS, 154, 259

Hummel, E. 1980, A&AS, 41, 151

Iglesias-Páramo, J. et al. 2006, ApJ, in press

Kennicutt, R.C. et al. 2003, PASP, 115, 928

Kong, X., Charlot, S., Brinchmann, J., & Fall, S.M. 2004, MNRAS, 349, 769

Kuchinski, L.E., Terndrup, D.M., Gordon, K.D., & Witt, A.N. 1998, AJ, 115, 1438

Martin, D.C. et al. 2005, ApJ, 619, L1

O'Connell, R.W. 1999, ARA&A, 37, 603

Panagia, N. 1973, AJ, 78, 9

Reach, W.T. et al. 2005, PASP, 117, 978

Rich, R.M. et al. 2005, ApJ, 619, L107

Rowan-Robinson, M. et al. 2005, AJ, 129, 1183

Sajina, A., Scott, D., Dennefeld, M., Dole, H., Lacy, M., & Lagache, G. 2006, MNRAS, in press

Schmitt, H.R., Calzetti, D., Armus, L., Giavalisco, M., Heckman, T.M., Kennicutt, R.C., Leitherer, C., & Meurer, G.R. 2006, ApJ, in press

Siebert, M. et al. 2005, ApJ, 619, L55

Wright, A. & Otrupcek, R. 1990, Parkes Catalogue, Australian Telescope National Facility

Yi, S.K. et al. 2005, ApJ, 619, L111

Yun, M.S., Reddy, N.A., & Condon, J.J. 2001, ApJ, 554, 803

Table 1. Infrared Flux Densities UPDATE MIPS NUMBERS!!!!!!!

Galaxy	3.6 μm (Jy)	4.5 μm (Jy)	5.8 μm (Jy)	8.0 μm (Jy)	24 μm (Jy)	70 μm (Jy)	160 μm (Jy)
NGC 0024	0.11 ±0.01	0.070±0.008	0.084±0.009	0.13 ±0.01	0.13 ±0.01	1.89 ±0.39	6.72 ±1.36
NGC 0337	0.10 ±0.01	0.066±0.007	0.13 ±0.01	0.37 ±0.04	0.65 ±0.07	8.84 ±1.77	18.30 ±3.69
NGC 0584	0.38 ±0.04	0.22 ±0.02	0.17 ±0.02	0.11 ±0.01	0.050±0.006	0.15 ±0.07	1.02 ±0.40
NGC 0628	0.90 ±0.09	0.54 ±0.06	1.16 ±0.12	2.68 ±0.27	3.09 ±0.31	29.75 ±5.96	116.65 ±23.34
NGC 0855	0.044±0.005	0.027±0.003	0.017±0.002	0.044±0.004	0.082±0.008	1.38 ±0.28	2.09 ±0.44
NGC 0925	0.32 ±0.03	0.21 ±0.02	0.35 ±0.04	0.61 ±0.06	0.90 ±0.09	12.21 ±2.45	39.53 ±7.95
NGC 1097	1.29 ±0.13	0.80 ±0.08	1.46 ±0.15	3.17 ±0.32	6.41 ±0.64	43.41 ±8.68	144.64 ±28.93
NGC 1266	0.056±0.006	0.042±0.004	0.051±0.005	0.087±0.009	0.85 ±0.08	9.65 ±1.93	9.14 ±1.84
NGC 1291	2.19 ±0.22	1.27 ±0.13	0.97 ±0.10	0.63 ±0.06	0.44 ±0.05	5.41 ±1.09	28.47 ±5.75
NGC 1316	2.57 ±0.26	1.53 ±0.15	1.13 ±0.11	0.55 ±0.06	0.36 ±0.04	4.22 ±0.85	9.66 ±1.94
NGC 1377	0.059±0.006	0.085±0.008	0.25 ±0.03	0.41 ±0.04	1.74 ±0.17	4.76 ±0.95	2.91 ±0.60
NGC 1404	0.76 ±0.08	0.43 ±0.04	0.32 ±0.03	0.16 ±0.02	0.083±0.009	0.15 ±0.09	0.31 ±0.18
NGC 1482	0.21 ±0.02	0.15 ±0.02	0.57 ±0.06	1.54 ±0.16	3.60 ±0.36	21.70 ±4.34	34.02 ±6.82
NGC 1512	0.40 ±0.04	0.24 ±0.02	0.26 ±0.03	0.43 ±0.04	0.42 ±0.04	5.40 ±1.08	21.85 ±4.38
NGC 1566	0.78 ±0.08	0.48 ±0.05	0.89 ±0.09	2.10 ±0.21	2.66 ±0.27	27.82 ±5.57	95.26 ±19.05
NGC 1705	0.026±0.003	0.018±0.002	0.009±0.002	0.016±0.001	0.052±0.005	1.09 ±0.22	1.20 ±0.25
NGC 2403	1.95 ±0.20	1.30 ±0.13	2.16 ±0.22	4.09 ±0.41	5.65 ±0.57	75.60 ±15.12	231.58 ±46.32
Holmberg II	0.074±0.008	0.056±0.006	0.030±0.004	0.024±0.004	0.17 ±0.02	3.18 ±0.64	4.05 ±0.87
M81 Dwarf A	0.002±0.001	0.001±0.001	<0.001	<0.001	...	...	...
DDO 053	0.005±0.001	0.004±0.001	0.002±0.001	0.007±0.001	0.028±0.003	0.31 ±0.07	0.32 ±0.11
NGC 2798	0.12 ±0.01	0.081±0.008	0.25 ±0.03	0.62 ±0.06	2.51 ±0.25	14.71 ±2.94	18.45 ±3.69
NGC 2841	1.32 ±0.13	0.75 ±0.08	0.65 ±0.07	1.15 ±0.12	0.88 ±0.09	8.66 ±1.74	54.87 ±10.98
NGC 2915	0.056±0.006	0.035±0.004	0.030±0.003	0.030±0.003	0.059±0.006	1.09 ±0.22	1.09 ±0.30
Holmberg I	0.012±0.001	0.008±0.001	0.007±0.002	0.007±0.001	0.013±0.004	0.33 ±0.12	0.76 ±0.23
NGC 2976	0.45 ±0.05	0.28 ±0.03	0.50 ±0.05	1.01 ±0.10	1.33 ±0.13	17.00 ±3.40	46.82 ±9.40
NGC 3049	0.042±0.004	0.027±0.003	0.060±0.006	0.13 ±0.01	0.41 ±0.04	2.28 ±0.46	4.05 ±0.82
NGC 3031	11.33 ±1.13	6.51 ±0.65	6.12 ±0.61	8.00 ±0.80	4.96 ±0.50	74.42 ±14.89	347.14 ±69.43
NGC 3034[a]	...	...	...	...	...	...	...
Holmberg IX	0.008±0.001	0.004±0.001	<0.006	<0.006	...	...	...
M81 Dwarf B	0.005±0.001	0.004±0.001	0.002±0.001	0.002±0.001	0.008±0.001	0.12 ±0.03	0.21 ±0.14
NGC 3190	0.39 ±0.04	0.23 ±0.02	0.23 ±0.02	0.32 ±0.03	0.26 ±0.03	4.34 ±0.87	13.19 ±2.65
NGC 3184	0.58 ±0.06	0.36 ±0.04	0.66 ±0.07	1.43 ±0.15	1.42 ±0.14	13.77 ±2.76	65.20 ±13.05
NGC 3198	0.28 ±0.03	0.17 ±0.02	0.33 ±0.03	0.68 ±0.07	1.03 ±0.10	8.68 ±1.74	34.96 ±7.00
IC 2574	0.16 ±0.02	0.090±0.009	0.065±0.007	0.066±0.007	0.27 ±0.03	4.61 ±0.92	10.31 ±2.12
NGC 3265	0.029±0.003	0.020±0.002	0.038±0.004	0.099±0.01	0.28 ±0.03	2.05 ±0.42	2.35 ±0.49
Markarian 33	0.027±0.003	0.019±0.002	0.049±0.005	0.13 ±0.01	0.82 ±0.08	3.34 ±0.67	3.46 ±0.71
NGC 3351	0.84 ±0.08	0.51 ±0.05	0.72 ±0.07	1.33 ±0.13	2.41 ±0.24	16.42 ±3.29	59.73 ±11.95
NGC 3521	2.12 ±0.21	1.35 ±0.14	2.55 ±0.26	6.23 ±0.62	5.37 ±0.54	49.87 ±9.98	206.67 ±41.35

Note. — The data are corrected for Galactic extinction (Schlegel, Finkbeiner, & Davis 1998) assuming $A_V/E(B-V) \approx 3.1$ and the extinction curve of Li & Draine (2001). The IRAC flux densities include the extended source aperture corrections provided in Reach et al. (2005), multiplicative factors of [0.944,0.937,0.772,0.737] at wavelengths [3.6,4.5,5.8,8.0] (μm). Flux uncertainties include both calibration and statistical uncertainties. Calibration errors are 10% at 3.6, 4.5, 5.8, 8.0, and 24 μm, and 20% at 70 and 160 μm.

[a]The bright core of NGC 3034 (M 82) has rendered the *Spitzer* data extremely difficult to process. Saturation effects severely limit our ability to extract reliable global flux densities.

Table 1. Infrared Flux Densities (continued)

Galaxy	3.6 μm (Jy)	4.5 μm (Jy)	5.8 μm (Jy)	8.0 μm (Jy)	24 μm (Jy)	70 μm (Jy)	160 μm (Jy)
NGC 3621	1.03 ±0.11	0.67 ±0.07	1.60 ±0.17	3.48 ±0.36	3.32 ±0.33	40.23 ±8.05	126.17 ±25.24
NGC 3627	1.94 ±0.19	1.24 ±0.12	2.37 ±0.24	5.54 ±0.55	7.26 ±0.73	68.94 ±13.79	208.14 ±41.63
NGC 3773	0.023±0.002	0.01 ±0.002	0.022±0.002	0.045±0.004	0.13 ±0.01	1.22 ±0.25	2.12 ±0.48
NGC 3938	0.33 ±0.03	0.21 ±0.02	0.40 ±0.04	0.97 ±0.10	1.05 ±0.11	12.14 ±2.43	46.78 ±9.36
NGC 4125	0.66 ±0.07	0.37 ±0.04	0.23 ±0.02	0.14 ±0.01	0.069±0.007	0.86 ±0.18	1.33 ±0.30
NGC 4236	0.26 ±0.03	0.21 ±0.02	0.11 ±0.01	0.21 ±0.02	0.53 ±0.05	7.08 ±1.42	18.87 ±3.85
NGC 4254	0.73 ±0.07	0.47 ±0.05	1.46 ±0.15	3.91 ±0.39	4.10 ±0.41	39.03 ±7.81	131.79 ±26.36
NGC 4321	0.99 ±0.10	0.64 ±0.06	1.20 ±0.12	2.86 ±0.29	3.33 ±0.33	32.29 ±6.46	128.41 ±25.68
NGC 4450	0.55 ±0.06	0.32 ±0.03	0.25 ±0.03	0.27 ±0.03	0.19 ±0.02	2.46 ±0.50	13.73 ±2.76
NGC 4536	0.41 ±0.04	0.29 ±0.03	0.60 ±0.06	1.64 ±0.17	3.38 ±0.34	22.49 ±4.50	54.39 ±10.89
NGC 4552	0.86 ±0.09	0.48 ±0.05	0.29 ±0.03	0.17 ±0.02	0.062±0.006	0.097±0.04	0.41 ±0.41
NGC 4559	0.37 ±0.04	0.23 ±0.02	0.41 ±0.04	0.83 ±0.08	1.08 ±0.11	14.32 ±2.87	46.81 ±9.37
NGC 4569	0.79 ±0.08	0.47 ±0.05	0.58 ±0.06	1.01 ±0.10	1.42 ±0.14	9.65 ±1.94	38.21 ±7.66
NGC 4579	0.90 ±0.09	0.52 ±0.05	0.51 ±0.05	0.72 ±0.07	0.74 ±0.07	8.21 ±1.65	39.07 ±7.82
NGC 4594	4.08 ±0.41	2.30 ±0.23	1.69 ±0.17	1.29 ±0.13	0.65 ±0.07	6.71 ±1.36	36.84 ±7.39
NGC 4625	0.05 ±0.005	0.030±0.003	0.055±0.005	0.13 ±0.01	0.13 ±0.01	1.70 ±0.34	4.70 ±0.95
NGC 4631	1.31 ±0.13	0.83 ±0.08	2.49 ±0.25	5.82 ±0.58	7.98 ±0.80	98.79 ±19.76	269.01 ±53.81
NGC 4725	1.18 ±0.12	0.70 ±0.07	0.75 ±0.08	1.20 ±0.12	0.81 ±0.08	7.48 ±1.50	53.42 ±10.70
NGC 4736	3.74 ±0.37	2.31 ±0.23	2.79 ±0.28	5.14 ±0.51	5.51 ±0.55	69.90 ±13.99	170.28 ±34.06
DDO 154	0.0042±0.0009	0.0030±0.0009	<0.0021	<0.0015	0.006±0.002	0.043±0.03	0.26 ±0.14
NGC 4826	2.62 ±0.26	1.57 ±0.16	1.65 ±0.17	2.33 ±0.23	2.48 ±0.25	35.69 ±7.14	85.39 ±17.09
DDO 165	0.016±0.002	0.012±0.001	0.005±0.002	0.004±0.001	0.011±0.003	0.14 ±0.05	0.27 ±0.15
NGC 5033	0.67 ±0.07	0.47 ±0.05	0.81 ±0.08	1.91 ±0.19	1.92 ±0.19	21.50 ±4.30	88.15 ±17.63
NGC 5055	2.47 ±0.25	1.54 ±0.15	2.68 ±0.27	5.61 ±0.56	5.60 ±0.56	59.77 ±11.96	286.35 ±57.27
NGC 5194	2.76 ±0.28	1.79 ±0.18	4.41 ±0.44	10.60 ±1.06	12.28 ±1.23	131.39 ±26.31	494.36 ±99.00
NGC 5195	0.86 ±0.09	0.51 ±0.05	0.43 ±0.04	0.63 ±0.06	1.31 ±0.13	10.86 ±2.17	12.34 ±2.49
Tololo 89	0.039±0.004	0.025±0.003	0.013±0.002	0.057±0.006	0.25 ±0.03	1.52 ±0.31	2.69 ±0.59
NGC 5408	0.053±0.006	0.037±0.004	0.039±0.004	0.037±0.004	0.42 ±0.04	2.95 ±0.59	2.21 ±0.49
NGC 5474	0.11 ±0.01	0.073±0.008	0.074±0.008	0.12 ±0.01	0.18 ±0.02	3.17 ±0.64	9.49 ±1.92
NGC 5713	0.21 ±0.02	0.14 ±0.01	0.27 ±0.03	1.13 ±0.11	2.28 ±0.23	17.23 ±3.45	34.77 ±6.96
NGC 5866	0.69 ±0.07	0.42 ±0.04	0.30 ±0.03	0.31 ±0.03	0.20 ±0.02	6.67 ±1.33	16.53 ±3.31
IC 4710	0.073±0.008	0.046±0.005	0.043±0.005	0.064±0.007	0.11 ±0.01	1.97 ±0.40	3.15 ±0.67
NGC 6822	2.20 ±0.22	1.38 ±0.14	1.49 ±0.15	1.41 ±0.14	2.54 ±0.25	53.30 ±10.67	136.27 ±27.28
NGC 6946	3.43 ±0.34	2.18 ±0.22	5.91 ±0.59	14.04 ±1.40	21.28 ±2.13	178.37 ±35.68	498.58 ±99.76
NGC 7331	1.67 ±0.17	1.02 ±0.10	1.83 ±0.18	4.01 ±0.40	3.94 ±0.39	56.53 ±11.31	164.14 ±32.83
NGC 7552	0.47 ±0.05	0.36 ±0.04	1.03 ±0.10	2.68 ±0.26	10.31 ±1.03	45.40 ±9.09	86.65 ±17.34
NGC 7793	0.80 ±0.08	0.47 ±0.05	1.03 ±0.10	1.83 ±0.18	1.97 ±0.20	29.86 ±5.98	119.54 ±23.92

Note. — The data are corrected for Galactic extinction (Schlegel, Finkbeiner, & Davis 1998) assuming $A_V/E(B-V) \approx 3.1$ and the extinction curve of Li & Draine (2001). The IRAC flux densities include the extended source aperture corrections provided in Reach et al. (2005), multiplicative factors of [0.944,0.937,0.772,0.737] at wavelengths [3.6,4.5,5.8,8.0] (μm). Flux uncertainties include both calibration and statistical uncertainties. Calibration errors are 10% at 3.6, 4.5, 5.8, 8.0, and 24 μm, and 20% at 70 and 160 μm.

Table 2. Ultraviolet, Optical, and Near-Infrared Flux Densities

Galaxy	E(B-V)	FUV 1528Å	NUV 2271Å	B 0.45 μm	V 0.55 μm	R 0.66 μm	I 0.81 μm	J 1.25 μm	H 1.65 μm	K_s 2.17 μm
	(mag)	(mJy)	(mJy)	(Jy)	(Jy)	(Jy)	(Jy)	(Jy)	(Jy)	(Jy)
NGC 0024	0.020	8.76 ±1.21	11.43 ±1.58	0.065	0.099	0.10	0.092	0.21	0.24	0.18
NGC 0337	0.112	10.46 ±1.45	18.69 ±2.59	0.055	0.042	0.17	0.029	0.18	0.19	0.16
NGC 0584	0.042	0.37 ±0.05	2.00 ±0.28	0.11	0.24	0.26	0.28	0.83	1.06	0.81
NGC 0628	0.070	75.96 ±10.52	99.23 ±13.74	0.51	0.74	0.71	0.62	1.50	1.62	1.25
NGC 0855[b]	0.071	1.81 ±0.25	3.25 ±0.45	0.027	0.041	···	···	0.087	0.10	0.080
NGC 0925	0.076	50.99 ±7.06	62.43 ±8.65	0.28	0.42	0.55	0.38	0.54	0.63	0.49
NGC 1097	0.027	36.26 ±5.19	50.97 ±7.18	0.41	···	···	0.78	2.19	2.59	2.13
NGC 1266	0.098	0.049±0.007	0.29 ±0.04	0.016	0.032	0.035	0.034	0.11	0.12	0.11
NGC 1291	0.013	7.38 ±1.02	16.28 ±2.26	0.60	1.30	1.27	1.41	3.96	4.24	3.65
NGC 1316	0.021	3.13 ±0.44	16.58 ±2.30	0.63	1.42	1.47	1.65	4.28	4.64	3.91
NGC 1377	0.028	···	···	0.010	0.020	0.020	0.031	0.092	0.11	0.088
NGC 1404	0.011	0.97 ±0.13	2.76 ±0.38	0.19	0.42	0.44	0.47	1.26	1.51	1.25
NGC 1482	0.040	0.41 ±0.06	1.43 ±0.21	0.019	0.040	0.049	0.049	0.21	0.29	0.27
NGC 1512	0.011	14.95 ±2.08	19.88 ±2.77	0.11	0.22	0.24	0.20	0.74	0.81	0.68
NGC 1566	0.009	54.49 ±7.59	65.52 ±9.07	0.33	0.27	0.28	0.33	1.27	1.34	1.18
NGC 1705[a]	0.008	···	16.76 ±2.32	0.029	0.037	0.033	0.025	0.052	0.051	0.041
NGC 2403[b]	0.040	258.11 ±35.74	307.45 ±42.57	1.33	1.68	···	···	2.66	2.83	2.26
Holmberg II	0.032	47.80 ±6.62	48.23 ±6.68	0.17	0.17	0.23	0.36	0.20	0.33	0.24
M81 Dwarf A	0.020	···	···	···	···	···	···	0.004	0.005	0.004
DDO 053	0.038	2.65 ±0.37	2.58 ±0.36	0.006	0.007	0.006	0.007	0.007	0.013	0.007
NGC 2798	0.020	1.12 ±0.16	2.33 ±0.32	0.034	0.066	0.066	0.085	0.15	0.18	0.16
NGC 2841	0.015	12.99 ±1.80	20.57 ±2.85	0.67	0.42	0.51	1.16	2.54	3.13	2.52
NGC 2915[b]	0.275	16.13 ±2.23	16.43 ±2.27	0.061	0.068	···	···	0.12	0.14	0.086
Holmberg I[b]	0.050	5.29 ±0.73	5.60 ±0.78	0.033	···	···	···	0.011	0.015	0.013
NGC 2976[a]	0.071	···	28.88 ±4.00	0.41	0.21	0.22	0.50	0.78	0.87	0.67
NGC 3049[a]	0.038	···	4.51 ±0.62	0.030	0.045	0.043	0.048	0.070	0.080	0.070
NGC 3031[b]	0.080	178.94 ±24.78	256.33 ±35.49	4.03	7.67	···	···	21.23	24.72	20.12
NGC 3034[b]	0.156	50.08 ±6.93	105.27 ±14.58	1.47	2.45	···	···	8.36	10.50	9.59
Holmberg IX[b]	0.079	4.01 ±0.56	5.00 ±0.69	0.011	0.010	···	···	0.034	0.032	0.024
M81 Dwarf B	0.081	0.75 ±0.10	0.92 ±0.13	···	···	···	···	0.011	0.014	0.013
NGC 3190	0.025	0.40 ±0.06	1.80 ±0.25	0.12	0.24	0.24	0.35	0.64	0.81	0.70
NGC 3184	0.017	···	···	0.53	0.63	0.65	1.04	0.95	1.11	0.86
NGC 3198	0.012	23.60 ±3.27	28.38 ±3.93	0.17	0.26	0.31	0.40	0.52	0.61	0.52
IC 2574	0.036	46.61 ±6.45	48.37 ±6.70	0.14	0.20	0.19	0.26	0.30	0.22	0.16
NGC 3265	0.024	0.57 ±0.08	0.96 ±0.13	0.012	0.021	0.012	0.023	0.046	0.056	0.045
Markarian 33	0.012	4.13 ±0.57	5.20 ±0.72	0.019	0.030	0.027	0.028	0.044	0.054	0.045
NGC 3351	0.028	17.66 ±2.45	28.77 ±3.98	0.36	0.51	0.66	0.94	1.52	1.72	1.45
NGC 3521	0.057	22.19 ±3.07	44.66 ±6.18	0.71	1.08	0.86	2.21	3.38	4.10	3.31

Note. — The data are corrected for Galactic extinction (Schlegel, Finkbeiner, & Davis 1998) assuming $A_V/E(B-V) \approx 3.1$ and the extinction curve of Li & Draine (2001). The uncertainties include both statistical and systematic effects.

[a]The far-ultraviolet detector was turned off during the observation.

[b]Optical data fromOptical data from the RC3 catalog (de Vaucouleurs et al. 1991).

Table 2. Ultraviolet, Optical, and Near-Infrared Flux Densities (continued)

Galaxy	E(B-V)	FUV 1528Å	NUV 2271Å	B 0.45 μm	V 0.55 μm	R 0.66 μm	I 0.81 μm	J 1.25 μm	H 1.65 μm	K_s 2.17 μm
	(mag)	(mJy)	(mJy)	(Jy)	(Jy)	(Jy)	(Jy)	(Jy)	(Jy)	(Jy)
NGC 3621[b]	0.081	76.91 ±11.20	110.23 ±15.76	0.49	0.69	···	···	1.77	2.04	1.57
NGC 3627	0.033	30.46 ±4.22	61.43 ±8.51	0.86	1.43	1.41	1.81	3.02	3.63	3.00
NGC 3773	0.027	···	···	0.020	0.029	0.026	0.029	0.041	0.038	0.035
NGC 3938[a]	0.021	···	36.41 ±5.04	0.25	0.38	0.32	0.40	0.58	0.56	0.51
NGC 4125[a]	0.019	···	3.44 ±0.48	0.33	0.21	0.24	0.58	1.26	1.49	1.22
NGC 4236[b]	0.015	63.45 ±8.79	76.24 ±10.56	0.43	0.53	···	···	0.57	0.81	0.54
NGC 4254	0.039	···	···	0.44	0.66	0.60	0.70	1.15	1.32	1.14
NGC 4321[a b]	0.026	···	54.04 ±7.48	0.45	0.71	···	···	1.69	1.95	1.56
NGC 4450[a]	0.028	···	5.39 ±0.75	···	···	···	···	1.09	1.35	1.02
NGC 4536	0.018	16.94 ±2.35	21.93 ±3.04	0.31	0.16	0.18	0.42	0.65	0.73	0.66
NGC 4552	0.041	···	···	0.21	0.43	0.45	0.56	1.48	1.75	1.38
NGC 4559	0.018	53.79 ±7.45	64.63 ±8.95	0.52	0.22	0.21	0.48	0.70	0.76	0.62
NGC 4569[b]	0.047	6.00 ±0.83	19.69 ±2.73	0.40	0.64	···	···	1.65	2.02	1.58
NGC 4579	0.041	···	···	0.58	0.33	0.37	0.98	1.85	2.17	1.72
NGC 4594	0.051	5.55 ±0.77	17.72 ±2.47	1.79	1.08	1.27	3.57	7.35	8.70	7.03
NGC 4625	0.018	6.04 ±0.84	7.97 ±1.10	···	···	···	···	0.088	0.11	0.085
NGC 4631	0.017	80.95 ±11.21	104.78 ±14.51	0.95	0.40	0.40	0.93	1.58	1.92	1.74
NGC 4725[b]	0.012	···	···	0.40	0.66	···	···	2.20	3.09	2.28
NGC 4736	0.018	67.19 ±9.30	91.87 ±12.72	1.43	2.45	2.57	3.23	6.28	7.46	6.09
DDO 154	0.009	4.54 ±0.63	4.42 ±0.61	0.009	0.010	0.008	0.008	0.009	0.012	0.011
NGC 4826	0.041	···	···	1.12	1.80	···	···	5.13	6.13	4.99
DDO 165	0.024	6.72 ±0.93	8.15 ±1.13	0.023	0.030	0.023	0.022	0.023	0.016	0.010
NGC 5033[b]	0.012	···	···	0.22	0.31	···	···	1.10	1.31	1.11
NGC 5055[b]	0.018	39.30 ±5.44	63.42 ±8.78	0.86	1.40	···	···	3.81	4.82	3.83
NGC 5194	0.035	160.03 ±22.16	260.75 ±36.10	1.17	1.72	2.04	2.88	4.51	5.72	4.28
NGC 5195	0.035	···	···	0.30	0.55	0.75	1.43	2.14	2.72	2.13
Tololo 89	0.066	7.57 ±1.05	11.35 ±1.57	···	···	···	···	0.074	0.063	0.050
NGC 5408[b]	0.068	···	···	0.073	0.098	···	···	0.17	0.16	0.10
NGC 5474[b]	0.011	24.35 ±3.37	27.18 ±3.76	0.14	0.18	···	···	0.13	0.15	0.11
NGC 5713[b]	0.039	5.16 ±0.71	10.02 ±1.39	0.091	0.13	···	···	0.34	0.38	0.31
NGC 5866	0.013	0.65 ±0.09	4.15 ±0.57	0.27	0.52	0.56	0.69	1.19	1.45	1.19
IC 4710	0.089	···	···	0.079	0.10	0.084	···	0.098	0.094	0.072
NGC 6822	0.231	···	···	0.81	0.76	0.32	0.50	5.16	5.34	3.96
NGC 6946[b]	0.342	···	···	2.24	2.90	···	···	6.57	5.31	5.35
NGC 7331	0.091	15.59 ±2.16	29.70 ±4.11	0.43	0.82	1.02	1.54	2.58	3.27	2.67
NGC 7552	0.014	7.73 ±1.07	15.15 ±2.11	0.14	0.23	0.23	0.22	0.65	0.76	0.65
NGC 7793	0.019	123.99 ±17.17	145.08 ±20.09	0.59	0.81	0.78	0.68	1.53	1.61	1.22

Note. — The data are corrected for Galactic extinction (Schlegel, Finkbeiner, & Davis 1998) assuming $A_V/E(B-V) \approx 3.1$ and the extinction curve of Li & Draine (2001). The uncertainties include both statistical and systematic effects.

[a]The far-ultraviolet detector was turned off during the observation.

[b]Optical data from the RC3 catalog (de Vaucouleurs et al. 1991).

Table 3. Submillimeter and Radio Flux Densities

Galaxy	450 μm (Jy)	850 μm (Jy)	450 μm Correction	850 μm Correction	20 cm (mJy)	20 cm reference
NGC 0024	···	···	···	···	···	
NGC 0337	···	0.35±0.05	···	···	110 ±11	1
NGC 0584	···	···	···	···	<50	2
NGC 0628	···	···	···	···	173 ±17	1
NGC 0855	···	···	···	···	4.9±0.5	3
NGC 0925	···	···	···	···	46 ± 5	1
NGC 1097	···	1.44±0.78	···	2.09	415 ±42	1
NGC 1266	···	···	···	···	116 ±12	1
NGC 1291	···	···	···	···	···	
NGC 1316	···	···	···	···	256 ±26	1
NGC 1377	···	···	···	···	<1.0	4
NGC 1404	···	···	···	···	3.9±0.6	3
NGC 1482	···	0.33±0.05	···	···	239 ±24	1
NGC 1512	···	···	···	···	7.0± 1	5
NGC 1566	···	···	···	···	400 ±40	7
NGC 1705	···	···	···	···	···	
NGC 2403	···	···	···	···	330 ±33	1
Holmberg II	···	···	···	···	20 ± 3	6
M81 Dwarf A	···	···	···	···	···	
DDO 053	···	···	···	···	···	
NGC 2798	···	0.19±0.03	···	1.08	83 ± 9	1
NGC 2841	···	···	···	···	84 ± 9	1
NGC 2915	···	···	···	···	···	
Holmberg I	···	···	···	···	···	
NGC 2976	···	0.61±0.24	···	1.56	51 ± 5	1
NGC 3049	···	···	···	···	12 ± 2	1
NGC 3031	···	···	···	···	380 ±38	1
NGC 3034	39.21±9.80	5.51±0.83	···	···	7660 ±770	1
Holmberg IX	···	···	···	···	···	
M81 Dwarf B	···	···	···	···	···	
NGC 3190	···	0.19±0.04	···	1.12	43 ± 5	1
NGC 3184	···	···	···	···	56 ± 5	1
NGC 3198	···	···	···	···	27 ± 3	1
IC 2574	···	···	···	···	11 ± 2	6
NGC 3265	···	···	···	···	11 ± 2	1
Markarian 33	···	0.04±0.01	···	···	17 ± 2	1
NGC 3351	···	···	···	···	44 ± 5	1
NGC 3521	···	2.11±0.82	···	1.56	357 ±36	1

Note. — Columns 4 and 5 list aperture correction factors for submillimeter flux densities, if necessary. See Dale et al. (2005) for details.

Note. — 20 cm references: 1–Yun, Reddy, & Condon (2001); 2–Hummel (1980); 3–Condon (1998); 4–Condon (1990); 5–Bauer et al. (2000); 6–Condon (1987); 7–Wright & Otrupcek 1990.

Table 3. Submillimeter and Radio Flux Densities (continued)

Band Galaxy	450 μm (Jy)	850 μm (Jy)	450 μm Correction	850 μm Correction	20 cm (mJy)	20 cm reference
NGC 3621	···	···	···	···	198 ±20	1
NGC 3627	···	1.86±0.70	···	1.53	458 ±46	1
NGC 3773	···	···	···	···	5.8±0.5	3
NGC 3938	···	···	···	···	62 ± 7	1
NGC 4125	···	···	···	···	<50 ±	2
NGC 4236	···	···	···	···	28 ± 3	1
NGC 4254	···	1.01±0.54	···	2.06	422 ±42	1
NGC 4321	···	0.88±0.49	···	2.19	340 ±34	1
NGC 4450	···	···	···	···	9.4± 1	3
NGC 4536	···	0.42±0.11	···	1.30	194 ±19	1
NGC 4552	···	···	···	···	100 ± 3	3
NGC 4559	···	···	···	···	65 ± 7	1
NGC 4569	···	0.47±0.08	···	1.11	83 ± 9	1
NGC 4579	···	0.44±0.07	···	···	98 ±10	1
NGC 4594	···	0.37±0.11	···	1.33	137 ±14	1
NGC 4625	···	···	···	···	7.1± 2	6
NGC 4631	30.70±10.02	5.73±1.21	1.27	1.17	1200 ±120	1
NGC 4725	···	···	···	···	28 ± 3	1
NGC 4736	···	1.54±0.66	···	1.67	271 ±27	1
DDO 154	···	···	···	···	···	
NGC 4826	···	1.23±0.31	···	1.24	101 ±10	1
DDO 165	···	···	···	···	···	
NGC 5033	···	1.10±0.55	···	1.93	178 ±18	1
NGC 5055	···	···	···	···	390 ±39	1
NGC 5194	···	2.61±0.39	···	···	1490 ±150	1
NGC 5195	···	0.26±0.04	···	···	50 ± 5	1
Tololo 89	···	···	···	···	4.2±0.8	3
NGC 5408	···	···	···	···	···	
NGC 5474	···	···	···	···	12 ± 2	6
NGC 5713	···	0.57±0.12	···	1.17	160 ±16	1
NGC 5866	0.79±0.20	0.14±0.02	···	···	23 ± 3	1
IC 4710	···	···	···	···	···	
NGC 6822	···	···	···	···	48 ± 5	1
NGC 6946	18.53±4.63	2.98±0.45	···	···	1395 ±140	1
NGC 7331	20.56±8.10	2.11±0.38	1.44	1.11	373 ±37	1
NGC 7552	···	0.80±0.17	···	1.17	276 ±28	5
NGC 7793	···	···	···	···	103 ±10	1

Note. — Columns 4 and 5 list aperture correction factors for submillimeter flux densities, if necessary. See Dale et al. (2005) for details.

Note. — 20 cm references: 1–Yun, Reddy, & Condon (2001); 2–Hummel (1980); 3–Condon (1998); 4–Condon (1990); 5–Bauer et al. (2000); 6–Condon (1987); 7–Wright & Otrupcek 1990.

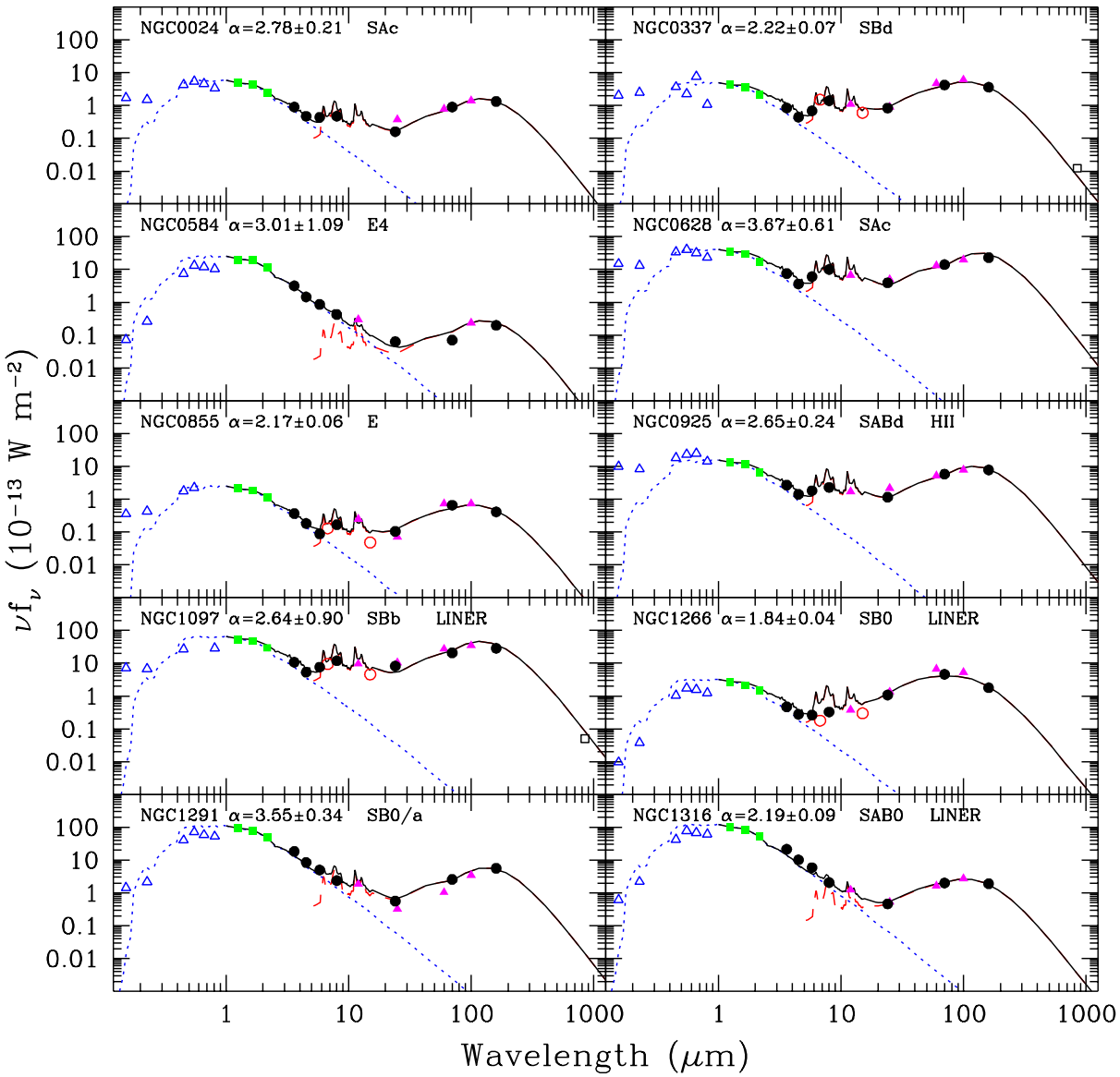

Fig. 1.— A presentation of the globally-integrated 0.15-850 μm spectral energy distributions for 10 SINGS galaxies. *GALEX* and optical, 2MASS, *Spitzer*, *IRAS*, *ISO*, and SCUBA data are represented by open triangles, filled squares, filled circles, filled triangles, open circles, and open squares, respectively. The solid curve is the sum of a dust (dashed) and a stellar (dotted) model. The dust curve is a Dale & Helou (2002) model fitted to the 24, 70, and 160 μm fluxes; the $\alpha_{\rm SED}$ listed within each panel parametrizes the distribution of dust mass as a function of heating intensity, as described in Dale & Helou (2002). The stellar curve is the 900 Myr continuous star formation, solar metallicity, Salpeter IMF ($\alpha_{\rm IMF} = 2.35$) curve from Vazquez & Leitherer (2005) fitted to the 2MASS data.

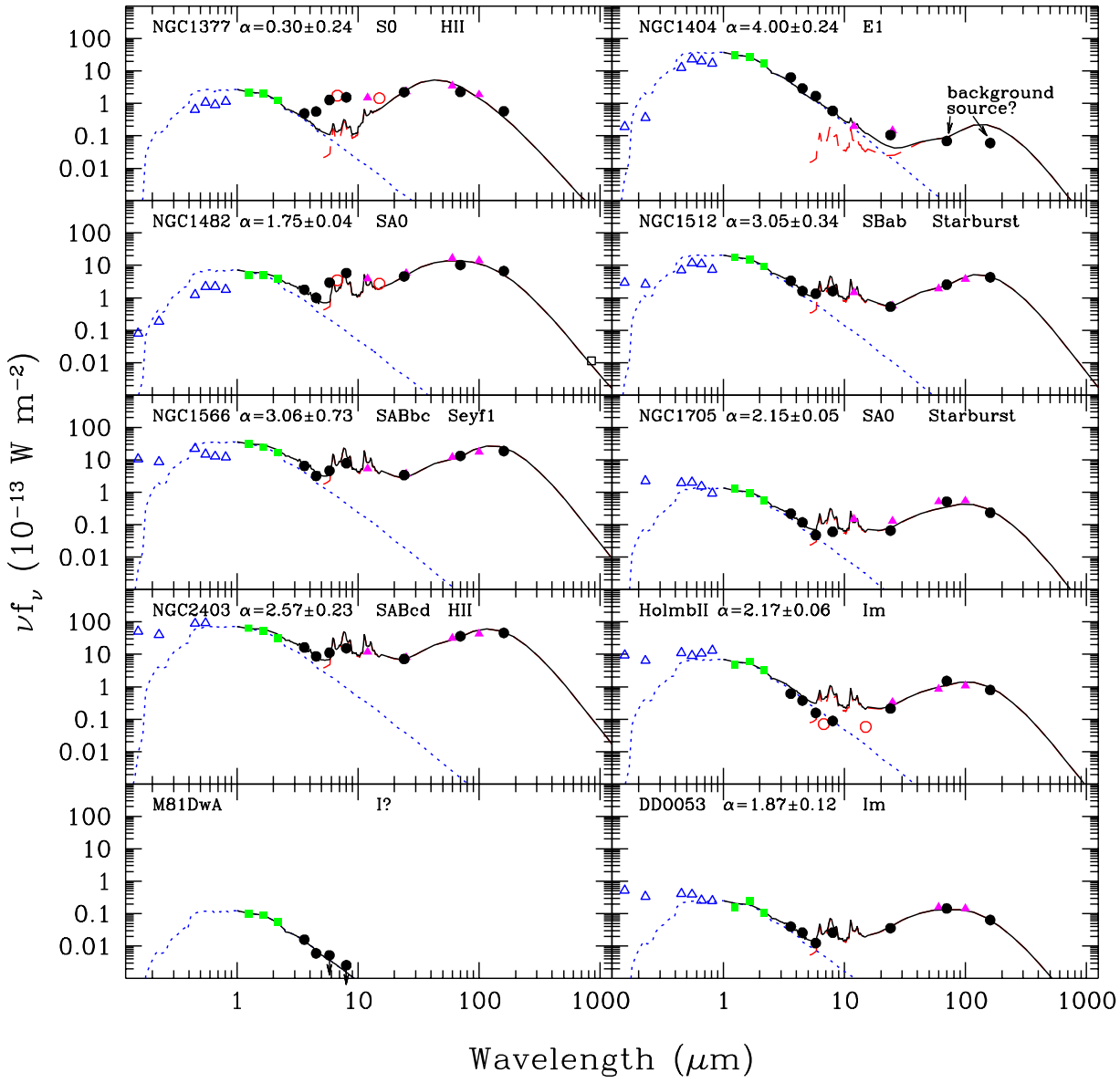

Fig. 2.— Similar to Figure 1 for 10 more SINGS galaxies.

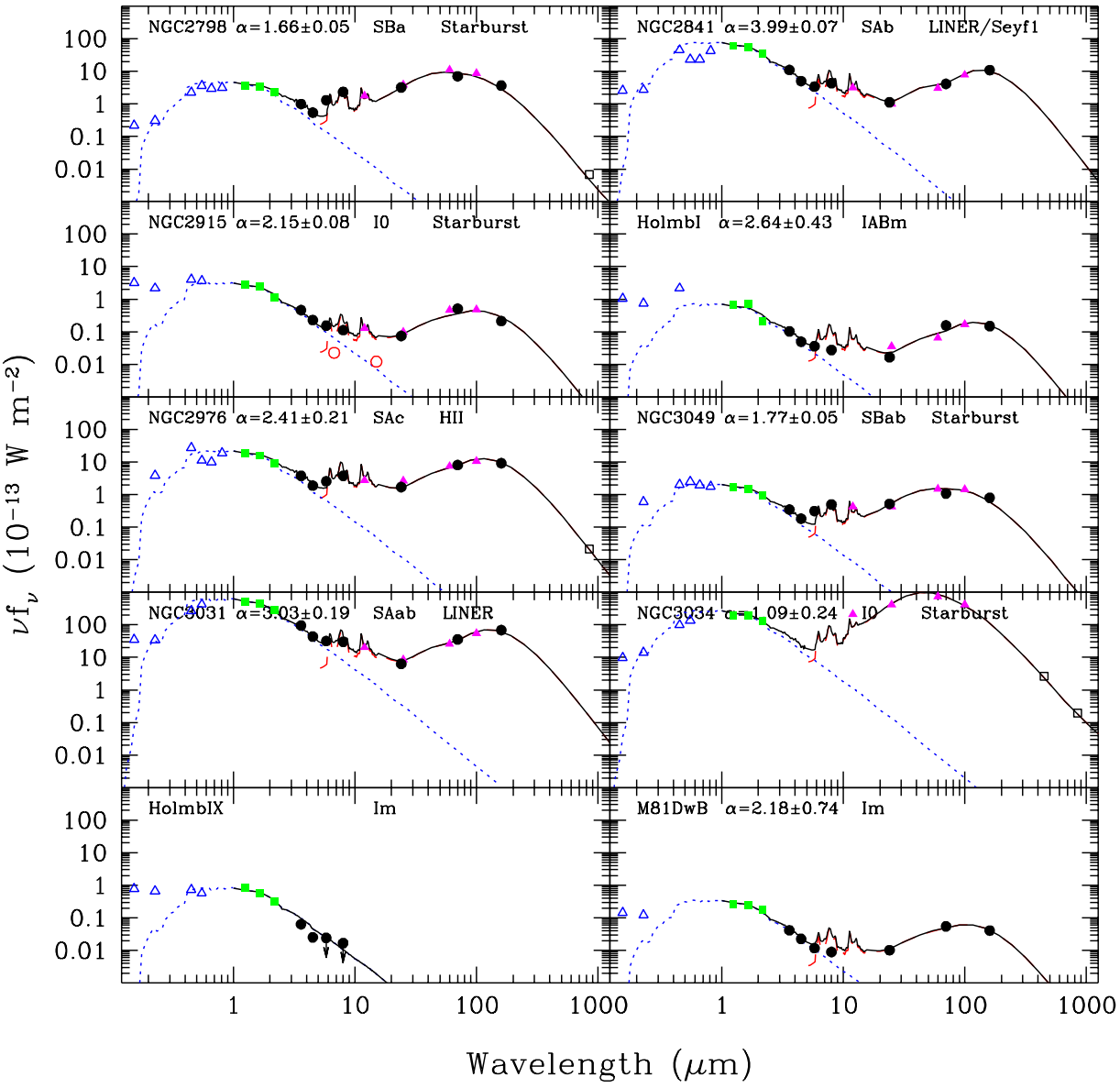

Fig. 3.— Similar to Figure 1 for 10 more SINGS galaxies.

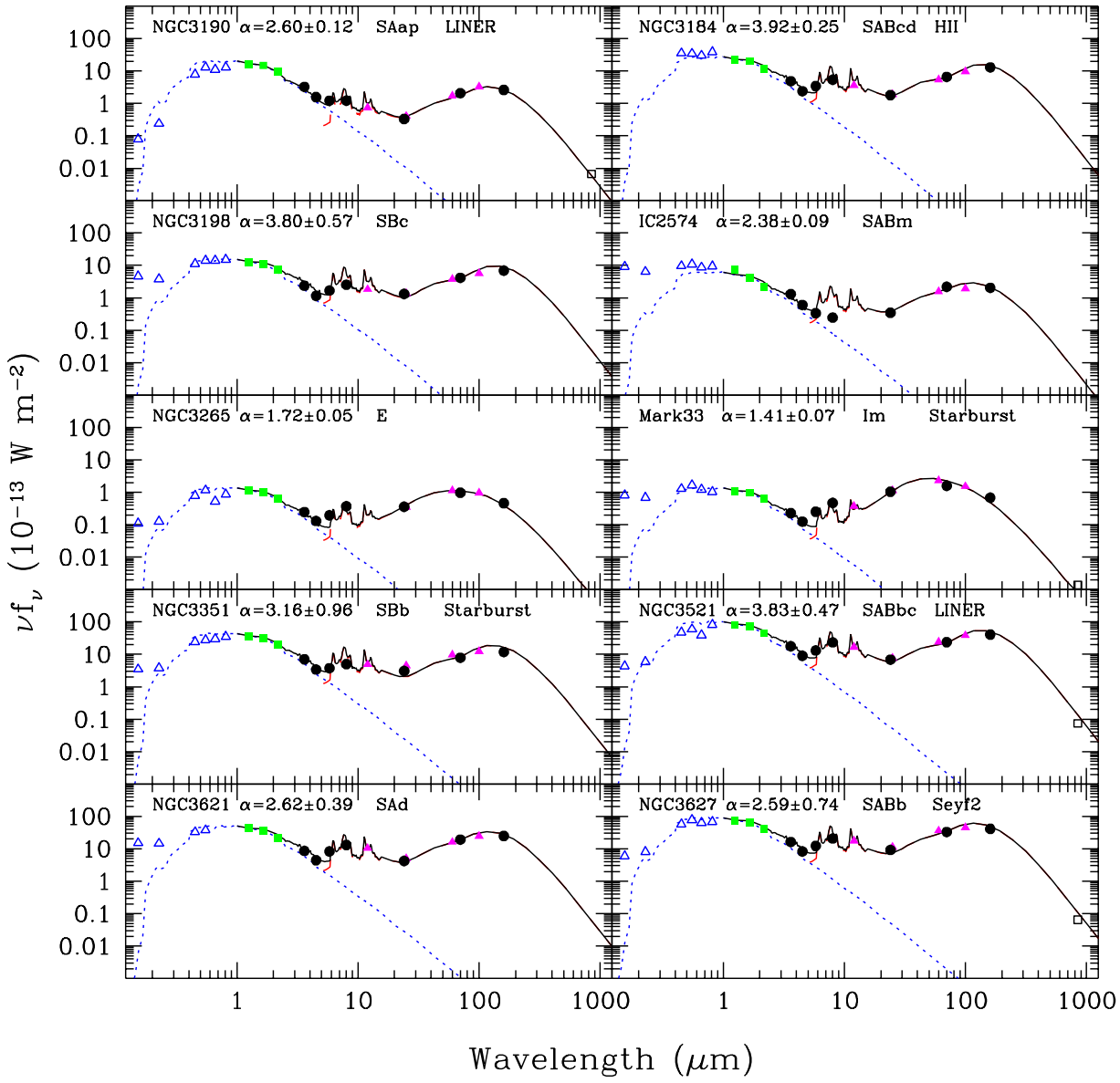

Fig. 4.— Similar to Figure 1 for 10 more SINGS galaxies.

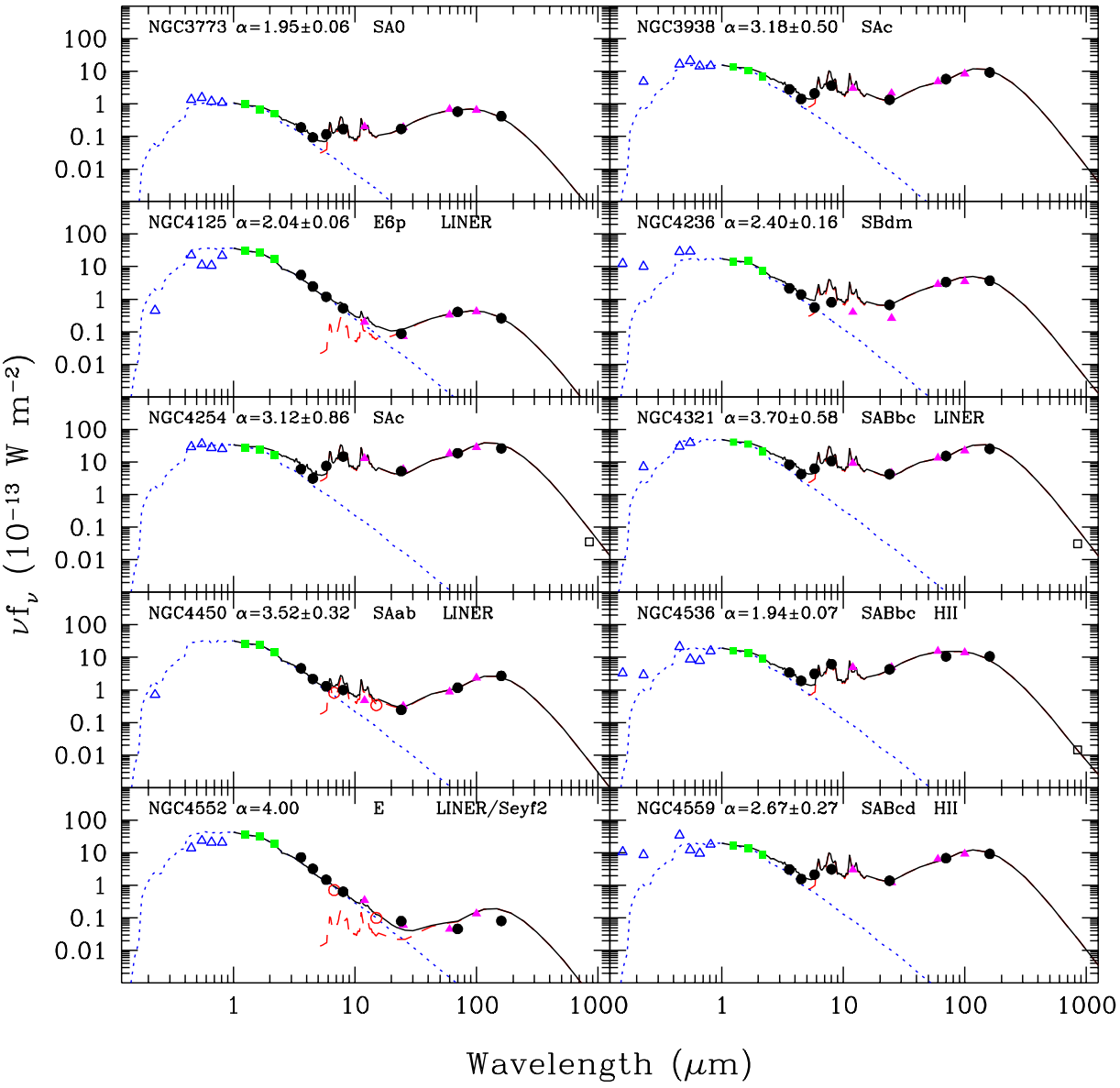

Fig. 5.— Similar to Figure 1 for 10 more SINGS galaxies.

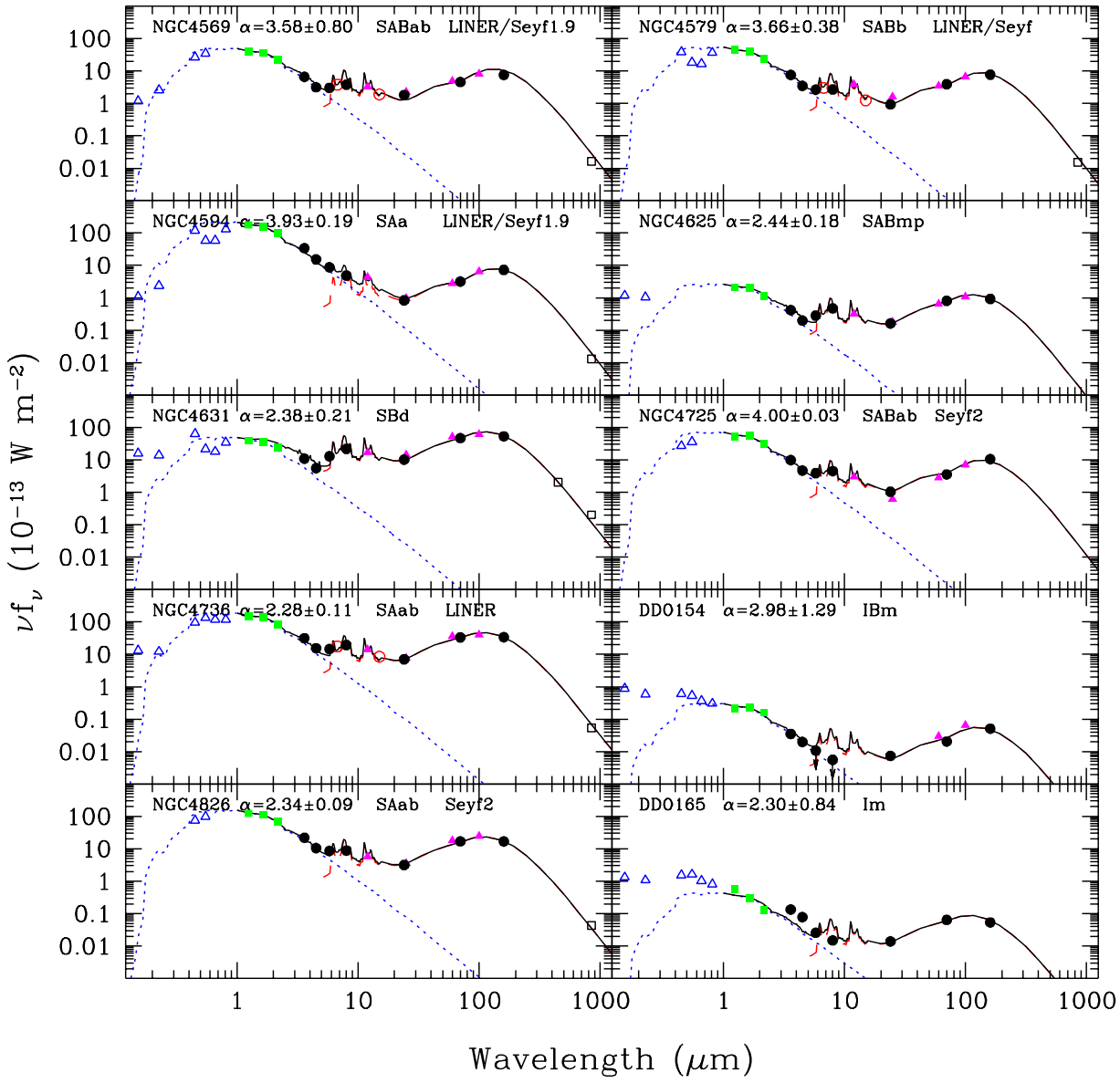

Fig. 6.— Similar to Figure 1 for 10 more SINGS galaxies.

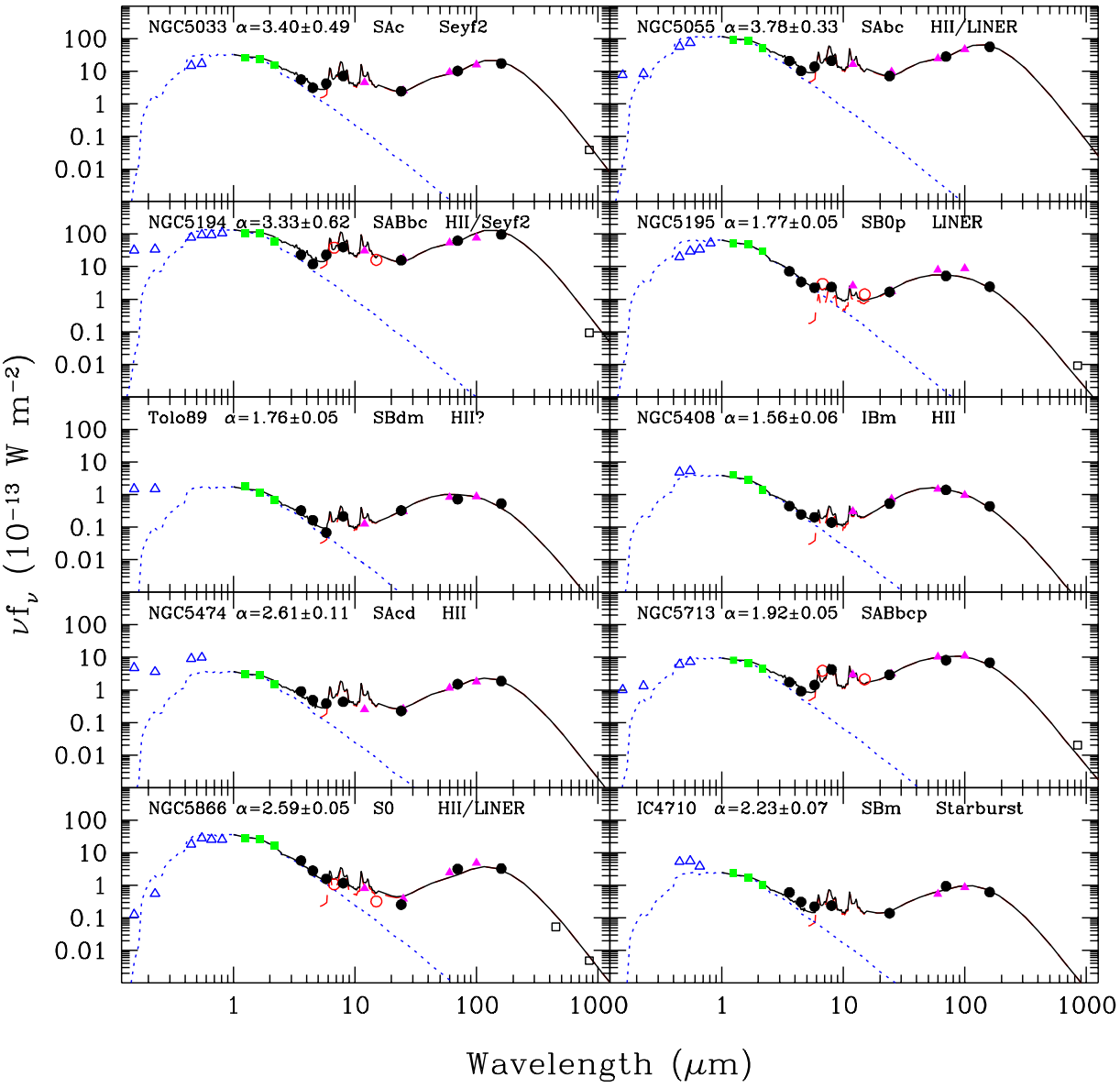

Fig. 7.— Similar to Figure 1 for 10 more SINGS galaxies.

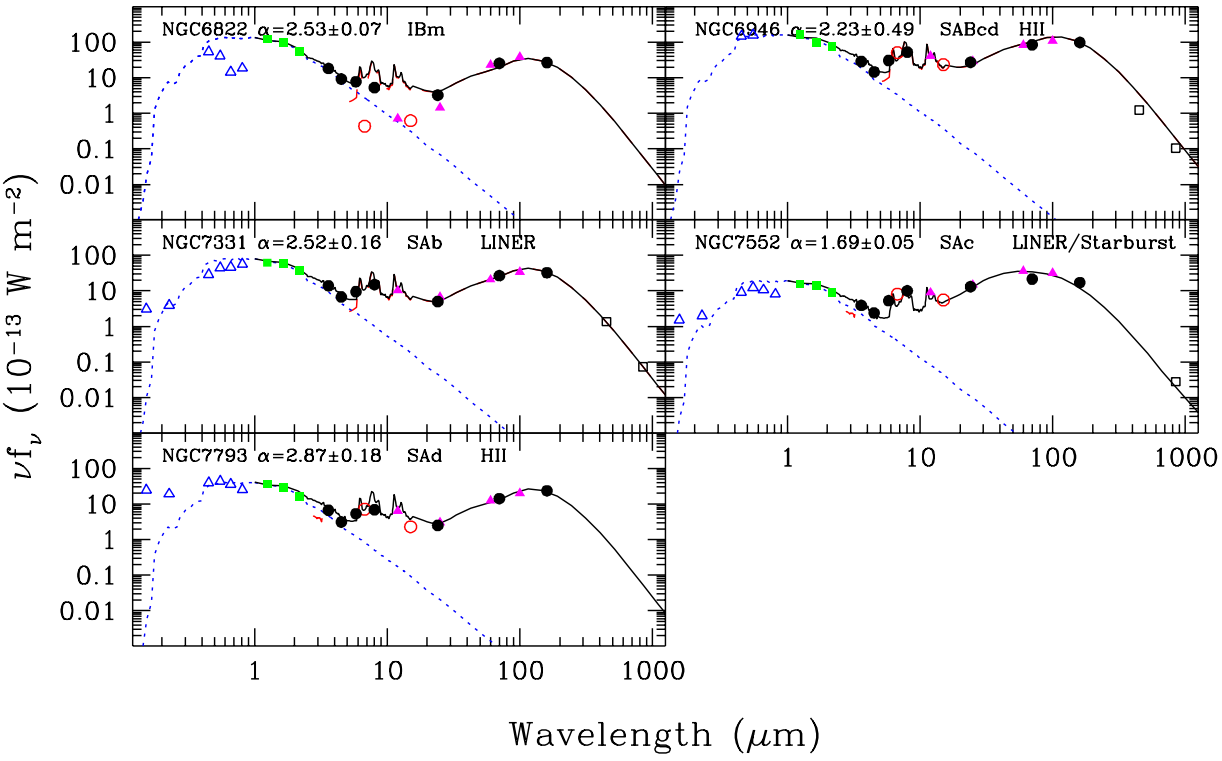

Fig. 8.— Similar to Figure 1 for 5 more SINGS galaxies.

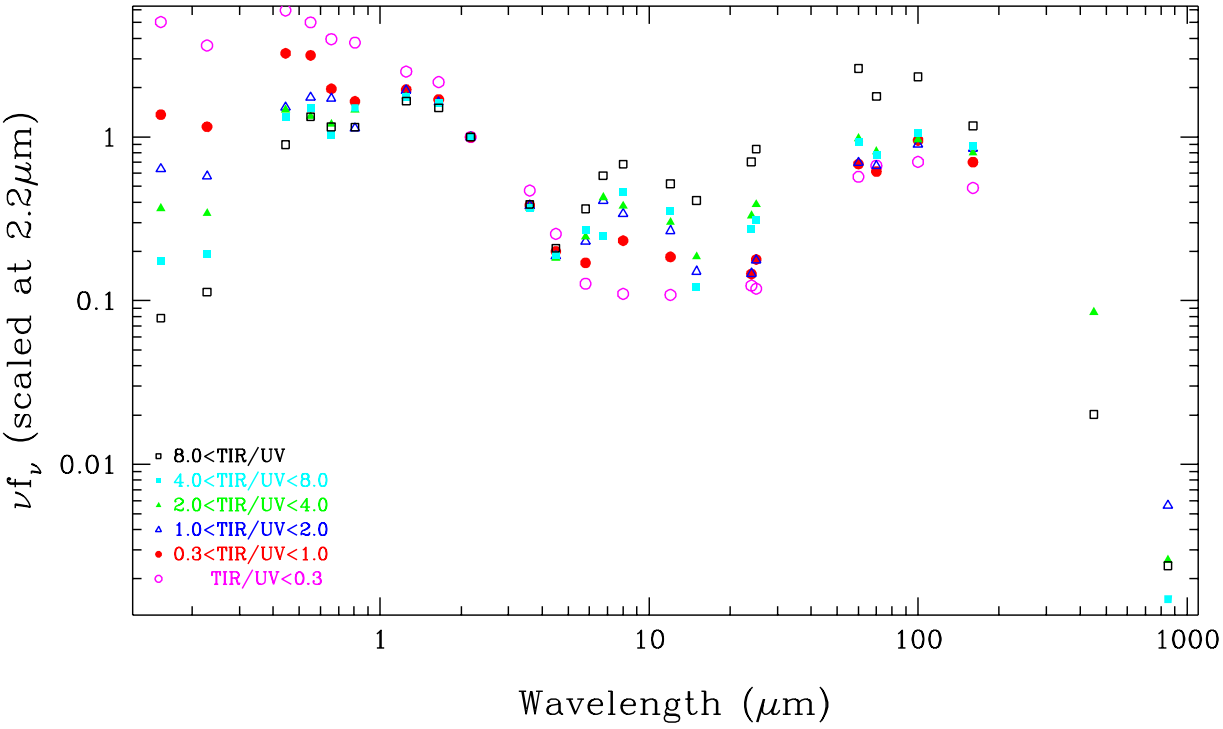

Fig. 9.— A display of stacked spectral energy distributions that emphasizes the infrared-to-ultraviolet variations within the SINGS sample. Each spectral energy distribution in the stack represents an average of approximately 10 individual spectral energy distributions that fall within a given bin of the infrared-to-ultraviolet ratio.

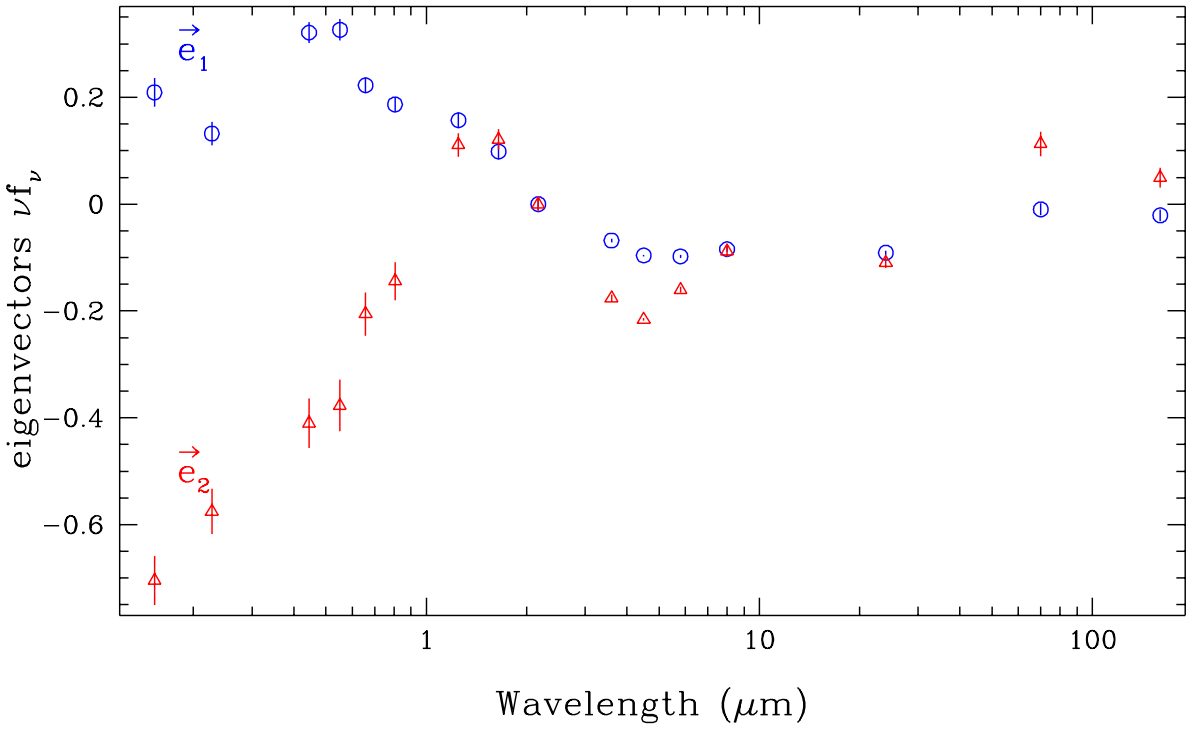

Fig. 10.— The strongest (circles) and second strongest (triangles) eigenvector spectra from a principal component analysis of the SINGS spectra are displayed. These are average eigenvectors stemming from 10,000 Monte Carlo simulations based on the observed fluxes (corrected for Galactic extinction) and their uncertainties; the error bars shown in this figure indicate the dispersion of the eigenspectra from the simulations. These eigenvectors have normalized eigenvalues of 0.84 and 0.10; $\langle\vec{e}_1\rangle$ and $\langle\vec{e}_2\rangle$ respectively contribute to 84% and 10% of the observed variation in the sample spectra.

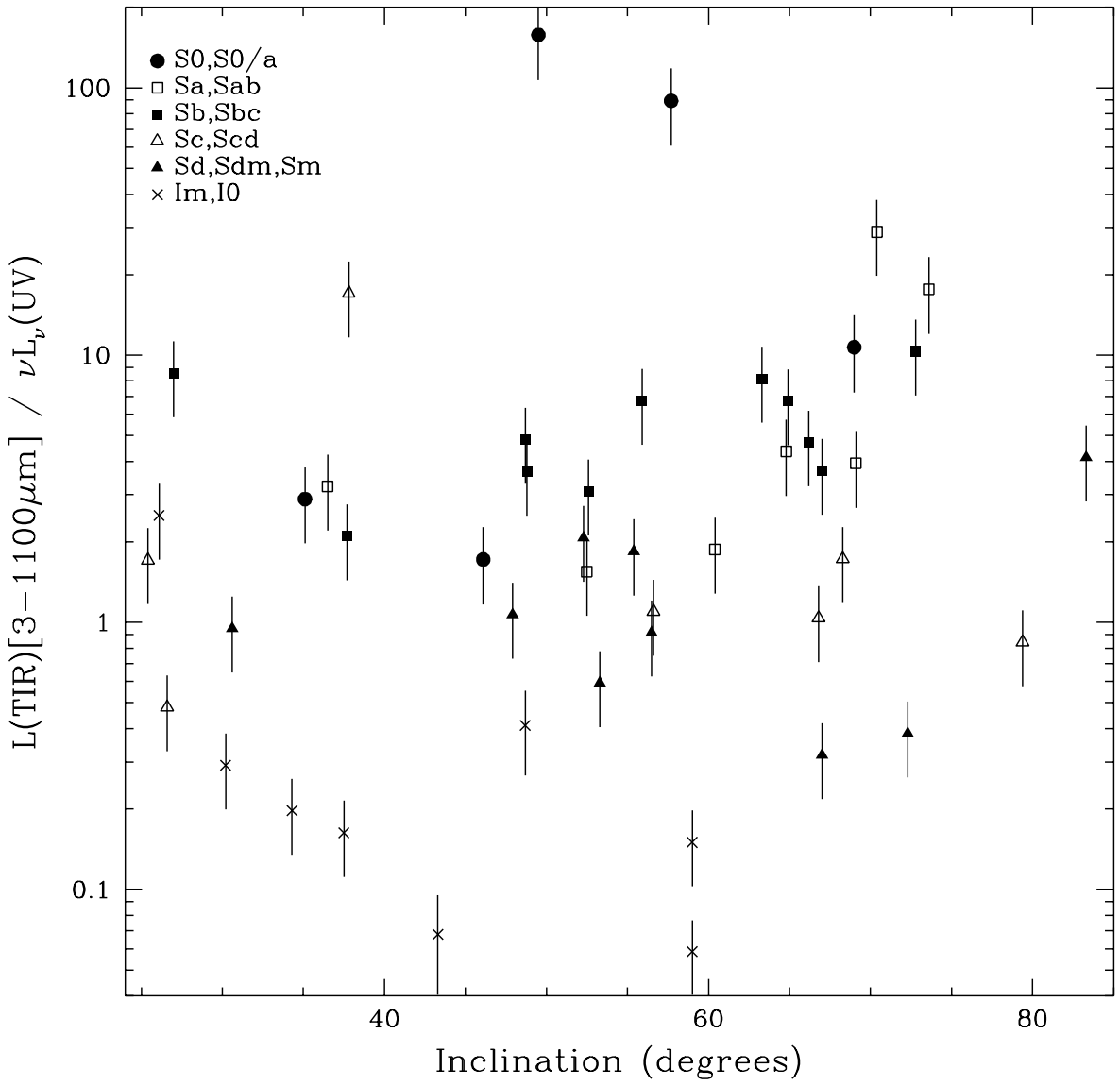

Fig. 11.— The infrared-to-ultraviolet ratio as a function of galaxy "disk" inclination. The ratio does not obviously trend with galaxy orientation.

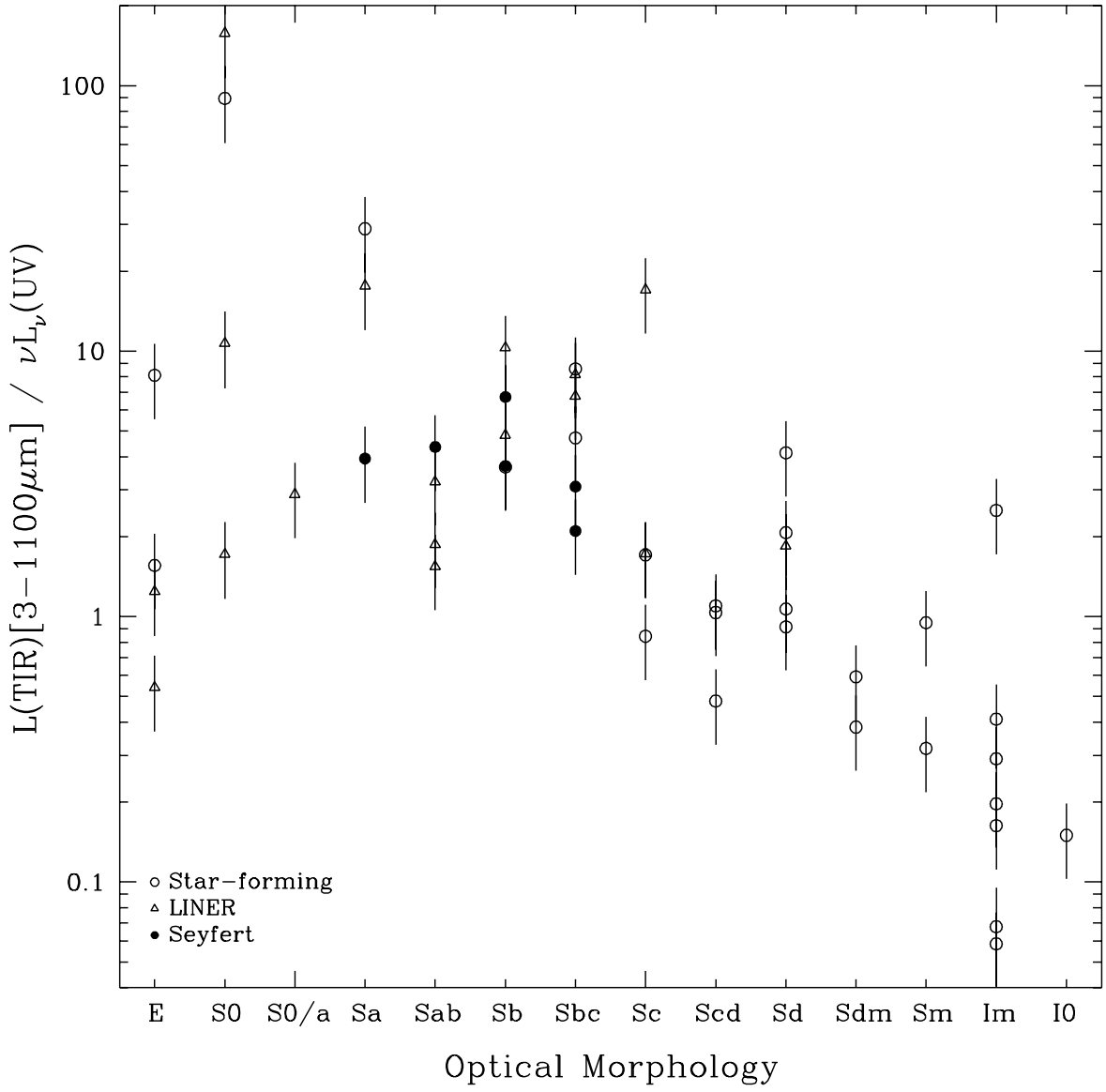

Fig. 12.— The infrared-to-ultraviolet ratio as a function of galaxy optical morphology. In general, the ultraviolet light increases in importance as the morphology changes from early-type spirals to late-type spirals to irregulars, reflecting the changing significance of star formation and the ultraviolet luminosity to the overall energy budget in galaxies.

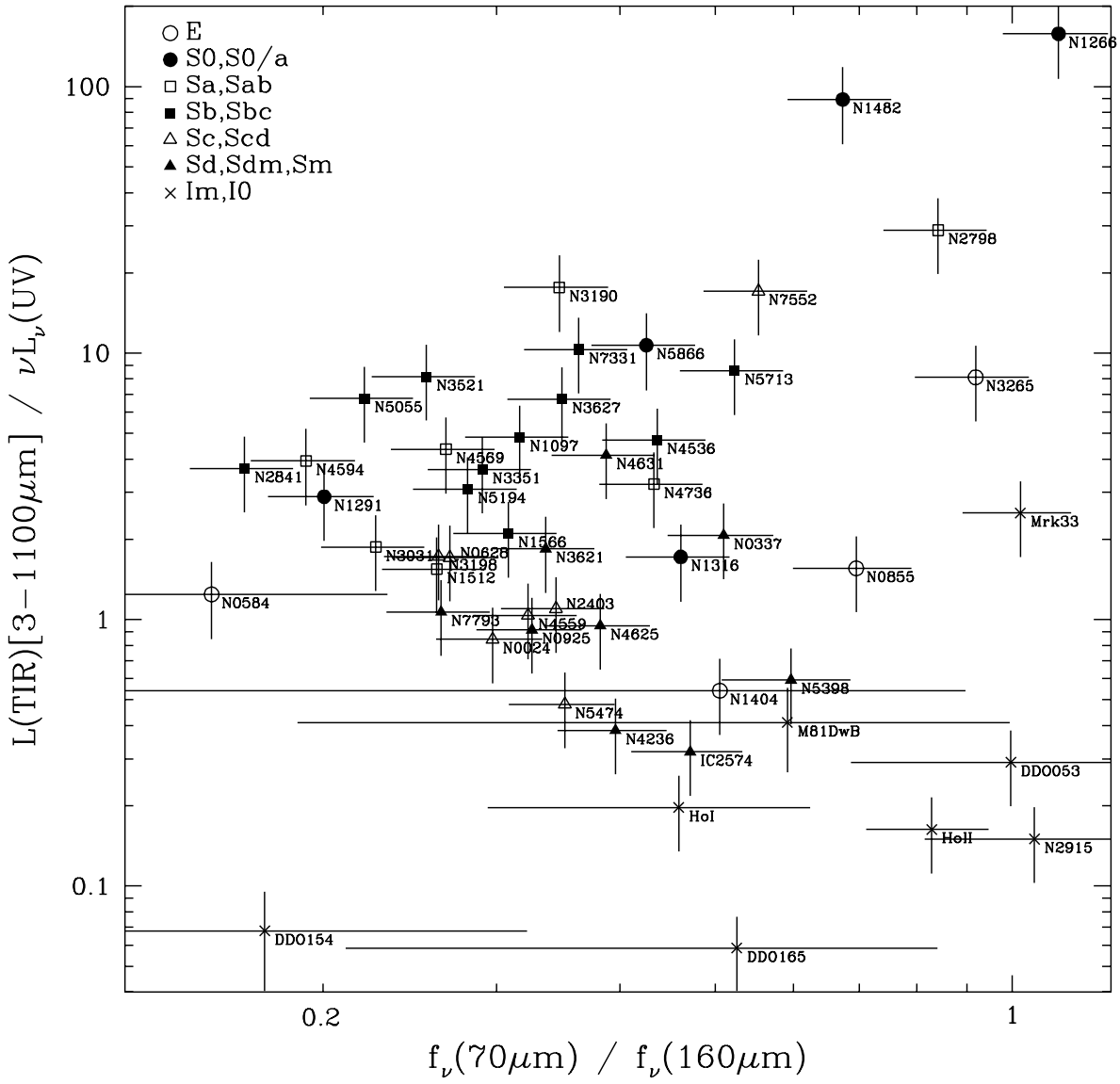

Fig. 13.— The infrared-to-ultraviolet ratio as a function of far-infrared color.

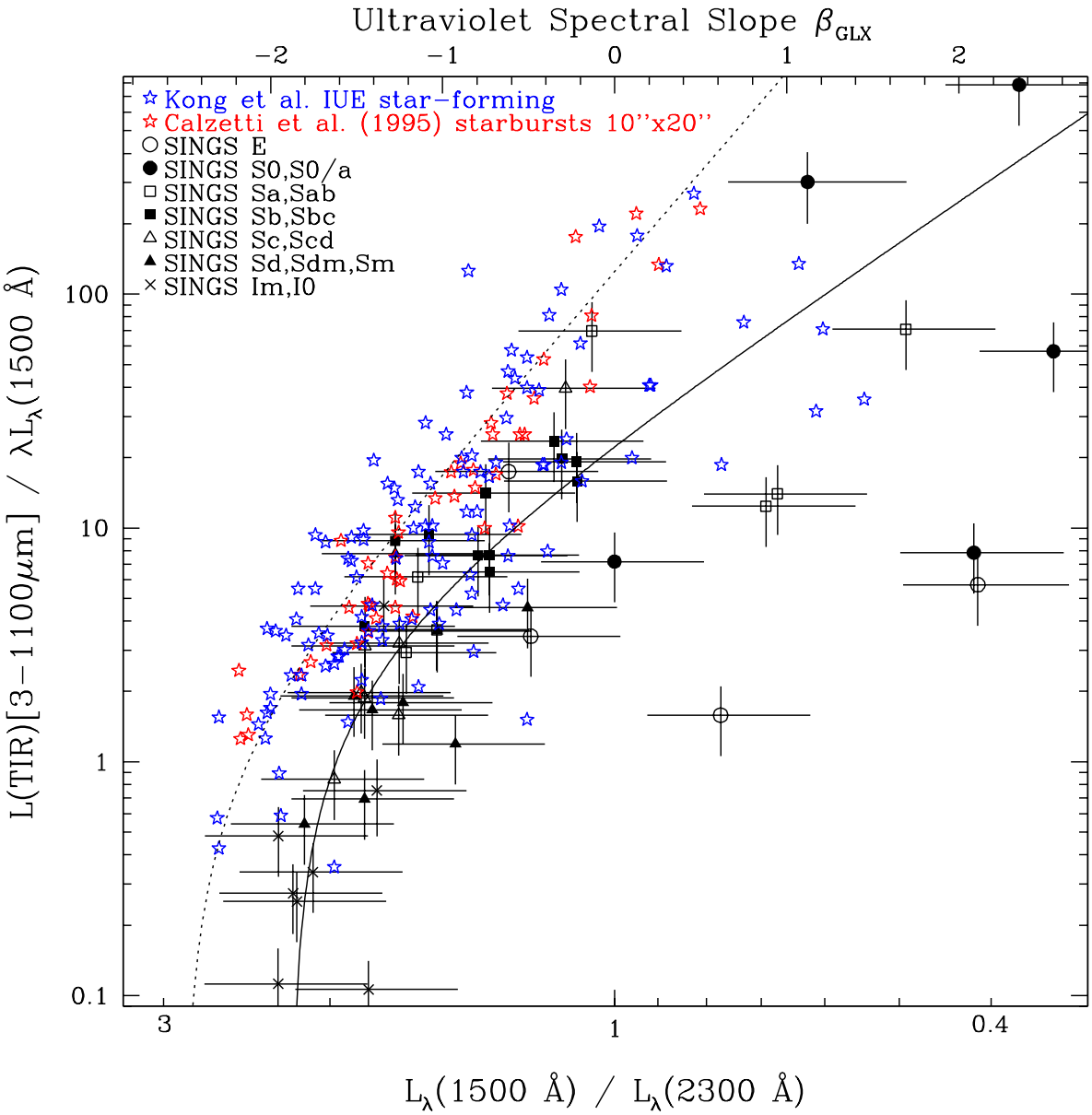

Fig. 14.— The infrared-to-ultraviolet ratio as a function of ultraviolet spectral slope. Normal star-forming and starbursting galaxies from Kong et al. (2004) and Calzetti et al. (1995) are plotted in addition to the SINGS data points. The dotted curve is that for starbursting galaxies from Kong et al. (2004) and the solid curve is applicable to normal star-forming galaxies (Cortese et al. 2006).